Dewey Ryan, M. (Orcid ID: 0000-0003-4437-0698)
Slavin James, A. (Orcid ID: 0000-0002-9206-724X)
Raines Jim, M (Orcid ID: 0000-0001-5956-9523)
Baker Daniel, N. (Orcid ID: 0000-0001-5909-0926)
Lawrence David, J. (Orcid ID: 0000-0002-7696-6667)

Energetic electron acceleration and injection during dipolarization events in Mercury's magnetotail

Ryan M. Dewey[1], James A. Slavin[1], Jim M. Raines[1], Daniel N. Baker[2], David J. Lawrence[3]

[1]Department of Climate and Space Sciences and Engineering, University of Michigan, Ann Arbor, MI, USA.

[2]Laboratory for Atmospheric and Space Physics, University of Colorado, Boulder, CO, USA.

[3]The Johns Hopkins University Applied Physics Laboratory, Laurel, MD, USA.

Corresponding Author: Ryan M. Dewey (rmdewey@umich.edu)

Key points:

1. 2976 magnetotail energetic electron events are identified in the GRS high-time-resolution measurements using an automated algorithm.
2. Dipolarization events are coincident with 538 of these electron events; dipolarizations display plasma depletion and dawn-dusk asymmetry.
3. Electrons undergo betatron and Fermi acceleration and may drift on Shabansky-like orbits while protons see modest betatron acceleration.

Index terms: Mercury (6235); Magnetotail (2744); Energetic Particles (7514); Particle Acceleration (7845)

Keywords: Mercury, dipolarization, injection, energetic electrons, magnetotail, substorm

Abstract

Energetic particle bursts associated with dipolarization events within Mercury's magnetosphere were first observed by Mariner 10. The events appear analogous to particle injections accompanying dipolarization events at Earth. The Energetic Particle Spectrometer (3 s resolution) aboard MESSENGER determined the particle bursts are composed entirely of electrons with energies ≤ ~300 keV. Here we use the Gamma-Ray Spectrometer high-time-resolution (10 ms) energetic electron measurements to examine the relationship between energetic electron injections and magnetic field dipolarization in Mercury's magnetotail. Between March 2013 and April 2015, we identified 2976 electron burst events within Mercury's magnetotail, 538 of which are closely associated with dipolarization events. These dipolarizations were detected on the basis of their rapid (~2 s) increase in the northward component of the tail magnetic field (ΔB_z ~ 30 nT), which typically persists for ~10 s. Similar to at Earth, we find these dipolarizations appear to be low-entropy, depleted flux tubes convecting planetward following the collapse of the inner magnetotail. We find electrons experience brief, yet intense, betatron and Fermi acceleration during these dipolarizations, reaching energies ~130 keV and contributing to nightside precipitation. Thermal protons experience only modest betatron acceleration. While only ~25% of energetic electron events in Mercury's magnetotail were directly associated with dipolarization, the remaining events are consistent with the Near-Mercury Neutral Line model of magnetotail injection and eastward drift about Mercury, finding that electrons may participate in Shabansky-like closed

drifts about the planet. Magnetotail dipolarization may be the dominant source of energetic electron acceleration in Mercury's magnetosphere.

1. Introduction

MESSENGER frequently observed energetic electrons ($E \gtrsim 10$ keV) within Mercury's magnetosphere [*Ho et al.*, 2011a, 2011b, 2012, 2016; *Lawrence et al.*, 2015; *Baker et al.*, 2016]. However, particle acceleration in this miniature magnetosphere has remained a topic of curiosity and controversy. While Mercury's intrinsic magnetic field forms a terrestrial-like magnetosphere when it interacts with the solar wind [e.g., *Alexeev et al.*, 2010; *Anderson et al.*, 2011], its magnetospheric dynamics operate on significantly smaller spatial scales and shorter temporal scales than the Earth's due to the many differences between the two magnetospheres [see, e.g., *Slavin et al.*, 2007, 2009, 2012]. The small physical scales limit the time an energetic particle can gain energy in Mercury's magnetosphere before being lost to surface precipitation or magnetopause shadowing, leaving little possibility for trapped radiation belts [*Slavin et al.*, 2007] and constraining possible acceleration mechanisms [*Zelenyi et al.*, 2007]. While electrons behave adiabatically, the magnetosphere's small size can result in nonadiabatic ion behavior and strong finite gyroradius effects [*Delcourt et al.*, 2010]. First detected by Mariner 10 [e.g., *Simpson et al.*, 1974], the presence of energetic particle bursts, therefore, raised questions about how such a small magnetosphere can rapidly accelerate particles to suprathermal and relativistic energies [e.g., *Baker et al.*, 2016].

Surveys of MESSENGER and Mariner 10 energetic particle bursts in Mercury's magnetotail suggest connection between particle acceleration and magnetic reconnection. Two of the Mariner 10 events during its first flyby appeared analogous to magnetic field dipolarization and particle injection events at Earth [*Christon et al.*, 1987]. A MESSENGER examination of the most intense energetic electron events detected by the Gamma-Ray Spectrometer revealed an additional example of simultaneous magnetic field dipolarization and energetic electron injection [*Baker et al.*, 2016]. At Earth, dipolarization events are rapid reconfigurations of the magnetotail into a more dipolar-state, i.e., the collapse of the near-tail region due to explosive nightside reconnection [e.g., *Runov et al.*, 2012]. The intense reconnection drives bursty bulk flows [e.g., *Angelopoulos et al.*, 1992] that carry the newly-reconnected dipolarizing flux bundle (DFB) [e.g., *Liu et al.*, 2013] toward the nightside inner magnetosphere. These flux bundles are interpreted as low entropy, depleted flux tubes or plasma bubbles created by the reconnection of low-β flux tubes between the north and south lobes of the magnetotail [e.g., *Sergeev et al.*, 1996]. As the flows brake near the inner magnetosphere, the magnetic field at the leading edge of the flux bundle steepens and forms a discontinuity (the dipolarization front, or DF) [e.g., *Runov et al.*, 2009]. Dipolarization events are a powerful source of particle acceleration, responsible for transporting energetic particles into the inner magnetosphere, where they are termed injection events [e.g., *Baker et al.*, 1978; *Deng et al.*, 2010; *Birn et al.*, 2011]. The planetward motion/braking of the dipolarization front energizes and heats the local plasma, while the bulk motion and collapse of the near-tail field transport particles into the inner magnetosphere [e.g., *Ashour-Abdalla et al.*, 2011; *Birn et al.*, 2013; *Gabrielse et al.*, 2016]. Magnetic field dipolarization associated

with energetic particle injection often occur during substorms at Earth [e.g., *Baker et al.*, 1996].

The MESSENGER spacecraft has observed brief, yet intense, substorm-like events and characteristic substorm features. In contrast to the Earth's several-hour process, Mercury's substorm-like events last only minutes [*Sun et al.*, 2015], but share common dipolarization [*Sundberg et al.*, 2012; *Sun et al.*, 2016] and tail loading/unloading [*Slavin et al.*, 2010] signatures with substorms at Earth. While a few examples of energetic electron events coincident with magnetic field dipolarization (here termed dipolarization-injection events) have been presented at Mercury [*Christon et al.*, 1987; *Baker et al.*, 2016], previous studies of energetic electron bursts with MESSENGER data have focused on the electrons and not the associated magnetospheric activity [e.g., *Ho et al.*, 2011a, 2011b, 2016; *Lawrence et al.*, 2015].

Here, we seek to expand upon the previous analyses of MESSENGER energetic electron bursts to discover the relationship between dipolarizations and injections at Mercury. As dipolarizations and injections relate to both magnetospheric and particle dynamics, in this study we focus on topics related to particle acceleration. In a companion study we focus on the magnetospheric dynamics and substorm characteristics of the dipolarization-injection events. The questions to be addressed in this study include:

1. Where and how frequently do dipolarization-injection events occur at Mercury?
2. What processes are responsible for energizing particles during these events at Mercury?
3. How responsible are these events for the energetic particle environment about Mercury?

We present statistical observations of injection events associated with magnetic field dipolarizations, suggesting frequent occurrence of rapid, intense electron acceleration associated with mechanisms similar to those operating during dipolarization events at Earth. Our investigation is organized as follows: in Section 2 we describe our data sources and event identification methodology; in Section 3 we present statistical analysis of the identified dipolarization-injection events; in Section 4 we discuss the results in context to previous Mercury studies and phenomena at Earth; and finally, in Section 5 we summarize our work and present avenues for future investigation.

2. Data Sources and Event Identification

2.1 MESSENGER Instruments

MESSENGER entered orbit about Mercury on 18 March 2011, and after providing over four years of continuous observations of the planet's surface and space environment, impacted the planet on 30 April 2015. For this investigation, we rely on the Magnetometer (MAG) [*Anderson et al.*, 2007], Fast Imaging Plasma Spectrometer [*Andrews et al.*, 2007], and Gamma-Ray Spectrometer (GRS) instruments [*Goldsten et al.*, 2007]. The MAG instrument measures the in situ vector magnetic field at 20 Hz (50 ms) time resolution. The FIPS sensor measures thermal and low-energy ions with energy per charge ratio (E/q) between < 50 eV/q and 13 keV/q, completing a scan at 0.1 Hz (10 s) nominally.

After a telemetry update on 25 February 2013, the GRS sensor provides a high-time-resolution proxy for energetic electron ($E \gtrsim 10$ keV) flux at 100 Hz (10 ms) resolution [see, e.g., *Baker et al.*, 2016]. Prior to the telemetry update, the GRS sensor mapped Mercury's surface composition by recording planetary nuclear fluorescence emissions [*Goldsten et al.*, 2007]. Its plastic scintillator anticoincidence shield (ACS) was designed to remove false positives recorded by the high-purity germanium crystal detector. The ACS responds to galactic cosmic rays (GCRs), planetary neutrons [*Peplowski et al.*, 2015], and energetic electrons [*Lawrence et al.*, 2015] impinging on the sensor's casing as well as gamma-rays emanating from the planetary surface and from the spacecraft. On 25 February 2013, the GRS telemetry was updated to send the 100 Hz ACS count rate data to the ground. The count rate consists of pulse-height analysis of photons in the ACS generated by the particles listed above [*Peplowski et al.*, 2015]. Planetary neutrons and Mercury-originating gamma-rays dominate the ACS count rate at low altitudes and for nadir boresight pointing, while GCRs and spacecraft-originating gamma-rays dominate the count rate at high altitudes and for off-planet boresight pointing. However, on the timescales of seconds, energetic electrons dominate the ACS count rate and appear as localized peaks superposed on the GCR/neutron background [*Lawrence et al.*, 2015]. While the precise field of view, response function, and energy threshold of the ACS are not well known, the GRS sensor possess a large geometric factor and is expected to behave nearly omnidirectionally [see *Lawrence et al.*, 2015]. In short, the count rate is derived from the ACS's response integrated over its omnidirectional field of view, large geometric factor, particle species (energetic electrons, GCRs, planetary neutrons), and particle energy. While the Energetic Particle Spectrometer (EPS, 3 s resolution) [*Andrews et al.*, 2007], X-Ray Spectrometer (XRS, 40 s resolution) [*Schlemm et al.*, 2007], and Neutron Spectrometer (NS, 20 s resolution) [*Goldsten et al.*, 2007] instruments also observe energetic electrons, we focus on GRS observations because of the sensor's superior time resolution and its high sensitivity from its nearly omnidirectional response and large geometric factor. For simplicity, we use "GRS" to refer to the high-time-resolution ACS measurements except where noted otherwise.

In addition to the 10-ms count rate, the GRS sensor also provides an energy-resolved count rate, but at a substantially lower time resolution (20 s). The energy-resolved count rate is derived from 20-s accumulations of individual pulse-height analysis events in the ACS. Similar to the 10-ms count rate, the spectral accumulations possess a background spectra dominated by planetary neutrons and GCRs; rapid enhancements above the background spectra are due to energetic electrons [*Peplowski et al.*, 2015]. The ACS has 1024 energy channels, each separated by approximately 3 keV. The instrument behaves non-linearly at lower (< 50 keV) energies and has an estimated threshold of ~10 keV [*Lawrence* et al., 2015]. The electron energy recorded in the 20-s spectral accumulations is the energy of the bremsstrahlung radiation produced by impinging elections; it is not the impinging electrons' kinetic energy, although the two are closely related [see *Goldsten et al.*, 2007; *Lawrence et al.*, 2015]. Assuming electrons deposit their entire kinetic energy in a single bremsstrahlung photon, we can estimate the electron energy spectra.

Our study uses the GRS high-time-resolution count rates and spectral accumulations collected between 1 March 2013 and 30 April 2015, corresponding to the interval between GRS telemetry update and planetary impact. During this interval, MESSENGER orbited the planet in a near-polar (~80° inclination), 8 h orbit. While MAG and FIPS operated continuously during this period of study, GRS only recorded the high-time-resolution count rate continuously when MESSENGER was within ~6600 km (i.e., 2.7 R_M, where R_M = 2440 km is Mercury's radius) of the planet's center. During the final months of the mission, there are additional gaps in the high-time-resolution GRS coverage associated with MESSENGER's final low-altitude campaign.

We use the Mercury solar magnetospheric (MSM) coordinate system to organize and display the spacecraft location, charged particle measurements, and vector magnetometer data. This right-handed coordinate system is centered at the origin of Mercury's magnetic dipole, which is offset ~484 km (~0.2 R_M) north of the planetary center [*Alexeev et al.*, 2010; *Anderson et al.*, 2011]. In this system, the X_{MSM}-axis points towards the Sun; the Y_{MSM}-axis lies in Mercury's orbital plane and points in the direction opposite to planetary motion; and the Z_{MSM}-axis completes the right-handed system (i.e., positive toward the north, which is parallel to the planetary rotation axis).

2.2 Dipolarization-injection event identification

We developed an automated algorithm to identify energetic electron events within the high-time-resolution GRS data [*Baker et al.*, 2016]. The algorithm, described in detail in Appendix A, uses a sliding window to determine the background GRS count rate and identifies electron events as points that fall significantly above the backgroundOver the 1 March 2013 to 30 April 2015 period of our study, the algorithm identified 10566 energetic electron events over 2139 orbits. The spatial distribution of these events about the planet as a function of local time (LT) and Z_{MSM} is shown in Figure 1. Figure 1 displays the number of electron events distributed about the planet corrected for MESSENGER's observation time, i.e., event frequency. The spatial distribution shares many similarities with previous studies of GRS [*Baker et al.*, 2016], XRS [*Ho et al.*, 2016] and NS electron events [*Lawrence et al.*, 2015]. We find the greatest frequency of electron events ~1 (2 min)$^{-1}$ near the magnetic equator in the post-midnight sector. At post-dawn, pre-noon local times, the electron events migrate to higher Z_{MSM}, before the frequency of events falls off sharply with local time in the post-noon and pre-midnight sectors. Few events are observed in the pre-midnight sector despite the almost uniform local time coverage of the MESSENGER spacecraft during the period of study. More events are observed north of Mercury's geographic equator ($Z_{MSM} \geq$ -0.2 R_M) due to MESSNGER's highly inclined orbit with periapsis near the planet's northern pole.

To identify dipolarization-injection events, we analyzed all electron events near the nightside plasma sheet for dipolarization signatures. We selected all electron events located behind the nightside of the planet ($X_{MSM} < 0$ R_M) and within 0.5 R_M of the magnetic equator ($|Z_{MSM}| \leq 0.5$ R_M), corresponding to the region outlined by the white dashed lines in Figure 1. Of the 10566 electron events, 2976 events (~30%) fall within this survey region. While dipolarizations at Earth are frequently associated with bursty bulk flows, characterized by

high-speed flows of 400 km/s or faster [e.g., *Angelopoulos et al.*, 1992], the FIPS sensor cannot directly observe sunward or antisunward flow in Mercury's magnetotail due to the obstruction of its field of view by the spacecraft's sunshade. As a result, we must rely on magnetic field observations to identify dipolarization events. Using similar criteria to *Sundberg et al.* [2012], we visually identified dipolarization fronts in the magnetic field for each electron event located within the survey region by (1) a sharp, step-like increase in B_z that (2) reaches a local maximum and is (3) followed by a gradual relaxation. For each dipolarization event, we define the dipolarization front (DF) Δt_{DF} to last from the minimum B_z prior to the step-like increase to the local maximum B_z at the end of the increase, the dipolarizing flux bundle (DFB) to last from the end of the DF to the minimum B_z following the event, and the dipolarization event Δt_{DIP} to last from the start of the DF to the end of the DFB. We use the term "dipolarization-injection event" to denote a dipolarization event coincident with an energetic electron event within the survey region. We refer to "injection events", in general, as the 2976 electron events within the survey region.

3. Dipolarization-Injection Event Observations and Analysis

3.1 Example dipolarization-injection events

Of the 2976 electron events within the survey region, we identified 538 dipolarization-injection events. Figure 2 through Figure 5 detail four sample MESSENGER dipolarization-injection events for comparison with the Mariner 10 events. We selected these four events to demonstrate the variability of magnetic field and particle signatures associated with dipolarization-injections at Mercury. Characteristic parameters from these examples are listed in Table 1.

In Figure 2, a dipolarization front begins at 13:08:17 (vertical dashed line) followed by an injection of energetic electrons less than a second later. The dipolarization front is marked by a sharp increase in B_z while the injection is marked by the sharp increase in the GRS count rate. The dipolarization front lasts until the maximum B_z at 13:08:19 (red tick), marking the beginning of the DFB that lasts until 13:08:38 (the end of the horizontal red line). The northward-component of the magnetic field B_z increases by nearly a factor of 15 over the dipolarization front (from 5.5 nT to 83.8 nT; ΔB_z = 78.3 nT), while the electron count rate increases by an order of magnitude during the dipolarization event, reaching a maximum near the middle of the dipolarization event at ~13:08:24 (from 550 s^{-1} to 6470 s^{-1}; δ_{peak} = 5920 s^{-1}, where δ is the background-subtracted 1-s smoothed GRS rate). During the DFB, additional magnetic field features correspond to particle signatures. Most easily seen in the unsmoothed GRS count rate (grey), the B_z depressions at ~13:08:21, ~13:08:23, and ~13:08:30 are coincident with a local maximum and two local minima in the GRS count rate, respectively, as marked by arrows. The unsmoothed GRS count rate falls to 0 s^{-1} during the second depression and falls to the background rate during the third depression. This substructure is attenuated in the 1-s smoothed GRS count rate (black). From the magnetic field signatures, this substructure could be interpreted as a series smaller dipolarizations embedded within the main event due to unsteady reconnection [e.g., *Fu et al.*, 2011, 2013]. The small, positive B_x throughout this interval and the coordinates of the spacecraft indicate

that MESSENGER was located slightly north of the central current sheet and in the post-midnight sector when the dipolarization passed over it. The dipolarization front lasts Δt_{DF} = 2.55 s, the dipolarization event lasts Δt_{DIP} = 21.2 s (spanned by the horizontal red line), and the injection lasts Δt_{GRS} = 13.3 s.

Neither the GRS spectral accumulations nor the FIPS H$^+$ spectrogram have sufficient temporal resolution to interpret fine plasma structure within this event, however, both contain several notable features. The spectral accumulation ending at ~13:08:05 represents the GRS background; it contains no electron events and is dominated by planetary neutrons and GCRs. Enhancements above the background in the two subsequent accumulations are due to energetic electrons. Compared to the background spectra, the first event accumulation (centered at 13:08:15) is enhanced from energies ~10 keV to ~180 keV and the second accumulation (centered at 13:08:36) is enhanced from energies ~10 keV to ~150 keV. While the first event accumulation observes electrons of greater maximum energy E_{max} than the second, the second contains more counts at energies below ~15 keV. Subtracting the background spectra and normalizing the residual spectra (not shown here) accentuates these trends. The first accumulation has a greater proportion of ~90-180 keV electrons while the second accumulation contains a greater proportion of ~10-30 keV electrons. The temporal resolution is too coarse to identify any dispersion signatures within the injection.

FIPS observations suggest some depletion and energization of thermal protons. Assuming the plasma distribution is sufficiently subsonic, we estimate the thermal plasma moments n and T [see *Gershman et al.*, 2013]. The scan centered at 13:08:05 precedes the dipolarization and observes the ambient plasma sheet with proton density n = 1.77 cm^{-3} and temperature T = 44.5 MK. The following scan covers the DF and notes a modest decrease in density (1.62 cm^{-3}) and increase in temperature (52.3 MK). The next scan (13:08:22 to 13:08:32) covers the DFB and observes no plasma, which could be an effect of plasma energized above the FIPS energy range, strong planetward flows shifting the plasma outside of FIPS's field of view, and/or due to the expected decreased density within DFBs [e.g., *Runov et al.*, 2015]. Comparing the ambient thermal plasma to the plasma within the DFB, $\Delta n/n$ = -1.00 and $\Delta T/T$ is undefined.

The dipolarization-injection events in Figure 3 display marked differences compared to the event in Figure 2. The interval in Figure 3 is comprised of three individual dipolarization-injection events, with the most significant at 07:59:32 marked by the dashed line and the other two marked by arrows. The first (main) event shows the largest change in the magnetic field and particle signatures with ΔB_z = 95.5 nT, δ_{peak} = 2670 s^{-1}, Δt_{DF} = 0.90 s, Δt_{DIP} = 13.0 s, and Δt_{GRS} = 15.6 s. At the beginning of the dipolarization front, B_z dips briefly below 0 nT. The injection signature appears substantially different compared to the event in Figure 2. The count rate rises slowly in the ~10 s preceding the dipolarization front and appears to repeatedly fall close to background levels during the dipolarization event. The GRS spectra for all three dipolarization-injection events appear similar. The two accumulations that span the three events both observe enhancements of energies to E_{max} ~ 140 keV compared to the background spectral accumulation ending at 07:59:20. Unlike the event in

Figure 2, the proportion of higher/lower energy electrons after subtracting the background spectra and normalizing the residual counts remains constant across the two accumulations. In other words, despite the first accumulation recording more counts than the second, both record identical electron spectra. Similar to the event in Figure 2, thermal protons increase in temperature and decrease in density throughout the series of events. Preceding the main dipolarization, $n = 1.99$ cm^{-3} and $T = 38.2$ MK in the ambient plasma sheet, followed by $n = 0.51$ cm^{-3} and $T = 67.9$ MK during the main DFB. Comparing the thermal plasma parameters, $\Delta n/n = -0.76$ and $\Delta T/T = 0.78$. The two secondary dipolarization events also observe plasma energization and depletion compared to the ambient plasma sheet but to a smaller degree; the FIPS scan centered at 07:59:51 observes $\Delta n/n = -0.70$ and $\Delta T/T = 0.14$. All three dipolarization-injection events in Figure 3 are located in the central plasma sheet, as noted by $B_x \sim 0$, and in the post-midnight sector.

The dipolarization-injection event in Figure 4 displays an energetic electron signature similar to the Mariner 10 events [*Christon et al.*, 1987]. The rapid rise of the electron count rate is coincident with the dipolarization front; the step-like increase in GRS count rate to a local maximum is followed by a general decay with some oscillation similar to the GRS electron event in Figure 4 of *Baker et al.* [2016]. The detrended count rate reaches a similar peak $\delta_{peak} = 5840$ s^{-1} to the event in Figure 2 although the change in the northward component of the magnetic field is more modest $\Delta B_z = 20.3$ nT. The difference in magnetic field signatures is related to the spacecraft's position during this interval. MESSENGER is located in the post-midnight sector and northward of the central current sheet, as indicated by $Z_{MSM} \sim 0.2\ R_M$ and the background $B_x \sim 40$ nT. Compared to the background accumulation ending at 00:31:20, both accumulations spanning the injection observe electron energies to $E_{max} \sim 170$ keV. Similar to the injection in Figure 2, the first accumulation during the injection observes a greater proportion of higher energy electrons (> 90 keV) while the second accumulation observes a greater proportion of lower energy electrons (< 20 keV) after accounting for the background GRS spectra. The thermal plasma observed during the DFB (scan centered 00:31:55) is less dense ($\Delta n/n = -0.46$) and hotter ($\Delta T/T = 0.12$) than the ambient plasma sheet (scan centered at 00:31:34). The timescales for this event are $\Delta t_{DF} = 2.60$ s, $\Delta t_{DIP} = 20.9$ s, and $\Delta t_{GRS} = 14.9$ s

The dipolarization-injection event in Figure 5 displays a modest enhancement in GRS count rate ($\delta_{peak} = 370$ s^{-1}) despite the northward component of the magnetic field increasing by $\Delta B_z = 85.8$ nT. Although smoothing the GRS count rate can attenuate substructure in injection events (e.g., Figure 2), it increases the signal-to-noise ratio for low-amplitude events, such as in this event. Similar to Figure 3, MESSENGER is located in the central current sheet and in the post-midnight sector during this interval, but did not observe a negative B_z at the start of the dipolarization front. For this event, $\Delta t_{DF} = 1.35$ s, $\Delta t_{DIP} = 15.9$ s, and $\Delta t_{GRS} = 2.0$ s. The GRS spectral accumulation spanning the injection observes slight enhancements at ~10-20 keV and ~40-80 keV compared to the preceding background spectra. FIPS observes plasma depletion and energization during the dipolarization compared to the ambient plasma. The observed density decreases $\Delta n/n = -0.46$ and the observed temperature

increases $\Delta T/T$ = 0.28 within the DFB compared to the ambient plasma (scans centered at ~21:09:05 and ~21:08:45, respectively).

3.2 Statistical dipolarization-injection analysis

To address the dipolarization-injection events statistically, Figure 6 displays the typical dipolarization-injection characteristics from all events. The top row contains parameters related to the dipolarization (ΔB_z, Δt_{DF}, Δt_{DIP}), the middle row contains parameters related to the injection (δ_{peak}, E_{max} Δt_{GRS}), and the bottom row contains parameters related to the thermal plasma ($\Delta n/n$, $\Delta T/T$). Distributions appear to resemble decaying exponential (δ_{peak}, Δt_{GRS}, $\Delta n/n$) or skewed unimodal functions (ΔB_z, Δt_{DF}, Δt_{DIP}, E_{max}, $\Delta T/T$). From the histograms, the average value of each parameter and its standard deviation after excluding outliers are: $\langle \Delta B_z \rangle$ = 28.0 ± 13.3 nT, $\langle \Delta t_{DF} \rangle$ = 2.01 ± 1.00 s, $\langle \Delta t_{DIP} \rangle$ = 10.5 ± 5.4 s, $\langle \delta_{peak} \rangle$ = 310 ± 190 s^{-1}, $\langle E_{max} \rangle$ = 120 ± 40 keV, $\langle \Delta t_{GRS} \rangle$ = 4.4 ± 4.0 s, $\langle \Delta n/n \rangle$ = -0.23 ± 0.65, and $\langle \Delta T/T \rangle$ = 0.20 ± 0.50. These averages are also listed in Table 1.

Given the substantial particle and magnetic field variability across the dipolarization-injection events, we performed superposed epoch analysis to understand better the typical characteristics, shown in Figure 7. We aligned each dipolarization-injection event at the midpoint of the dipolarization front and averaged the GRS, FIPS, and MAG observations. Since the GRS count rate and MAG vector field have time resolutions significantly shorter than the typical dipolarization front, both are analyzed and plotted at their native resolutions. Since the GRS spectral accumulations and FIPS scans have time resolutions significantly longer than the typical dipolarization front, both are oversampled at 1 s resolution. Time is plotted in seconds; we performed no time normalization on the MESSENGER observations. For the GRS rate and MAG vector field, the shaded regions correspond to the standard deviation of the mean multiplied by a factor of 5 for visibility, and the black horizontal dashed lines represent the pre-event value, each parameter averaged over -30 ≤ t ≤ -5 s. The red horizontal dashed line is the propagated Poisson error from the background at the 5-sigma level, akin to the GRS event algorithm significance level (see Appendix A). For the B_x and B_y components, we averaged the absolute value of these parameters to determine the typical offset from zero. For the GRS spectral accumulation, we display the statistically-significant relative change from the average GRS spectra over the range -20 < t < -10 s to highlight features and remove artifacts from the non-linearity below ~50 keV. To construct the FIPS H$^+$ E/q spectrogram, we superposed FIPS energy-resolved pitch angle distributions at each time step and integrated the superposed distributions over pitch angle to obtain the E/q spectra. We also show the proton density as a function of time.

The superposed epoch B_z and GRS count rate share nearly identical temporal profiles. Both B_z and the count rate begin decreasing from background levels at approximately t = -4 s, reaching a minimum at $t \approx$ -1 s and rising to a maximum at $t \approx$ +1 s. The dipolarization front lasts for Δt_{DF} = 1.75 s and results in ΔB_z = 19.8 nT. The GRS count rate increases to δ_{peak} = 446 s^{-1} over the background count rate. After the dipolarization front, B_z decays smoothly until reaching a constant value at $t \approx$ +7 s; the entire dipolarization event lasts Δt_{DIP} = 8.2 s. The magnitude of B_z at the end of the interval (48.0 nT) is greater than at the beginning (43.2 nT),

consistent with the plasma sheet thickening expected with dipolarization events. The changes in B_z are captured in the total field strength B. Throughout the interval, $|B_x|$ and $|B_y|$ remain at near-constant values (~22 nT and ~13 nT, respectively) while the average B_x and B_y (not shown here) each display no features and remain at ~0 nT.

While the magnetic field decays smoothly following the dipolarization front, the energetic electron count rate exhibits additional behavior. Following the peak at $t \approx +1$ s, the GRS count rate decays slowly to background values with $\Delta t_{GRS} = 11.0$ s, but exhibits a secondary maximum at $t \approx +17$ s. This secondary maximum is not reflected in the magnetic field signature, suggesting that this peak may be due to MESSENGER interacting with either the same population of electrons as they drift about the planet or another population entirely. This peak, however, falls below the 5-sigma significance level (red) and would not be identified as an electron event by the GRS algorithm.

The GRS spectra observe a dispersionless injection with the count rate of energies < 100 keV increasing nearly simultaneously at $t \approx -3$ s. In fact, the GRS spectra show a slight inverse dispersion of energies > 100 keV. During the injection, we observe an increase in electron energies up to 130 keV. Energies > 20 keV reach a maximum change at the end of the dipolarization front at $t \approx +2$ s, while energies < 20 keV reach a maximum change during the DFB at $t \approx +8$ s, as indicated by the black line. We observe the greatest change in the spectra at these lower (< 20 keV) energies. The trend of lower energies reaching a maximum change later than higher energies is similar to the dipolarization-injection events in Figures 2 and 4. In these events, we observe the greatest proportion of lower energy electrons later in the event.

FIPS observes plasma depletion and energization during the superposed dipolarization-injection. The proton density begins decreasing from 0.85 cm^{-3} at $t \approx -4$ s to a minimum of 0.59 at $t \approx +6$ s during the DFB. Following the minimum, the density increases slowly to pre-event values. To assess plasma energization in detail, we examine the superposed FIPS energy-resolved pitch angle distributions used to construct the H$^+$ E/q spectrum in Figure 7. Figure 8 contains the superposed energy-resolved pitch angle distributions averaged over intervals before ($-20 < t < -10$ s) and during ($0 < t < 10$ s) the superposed dipolarization-injection. Each pitch-angle energy bin is sufficiently sampled for statistical analysis; the minimum number of observations in a single bin is 86, the maximum is 510, and the average is 358. Computing the plasma moments of each distribution, the H$^+$ density decreases from 0.87 cm^{-3} prior to the dipolarization event to 0.61 cm^{-3} during the event ($\Delta n/n = -0.30$). The decrease in density is readily noted within the black boxes. The distributions also indicate a modest energization and heating of protons; the temperature increases from 35.2 MK prior to the event to 38.0 MK during the event ($\Delta T/T = 0.08$). The change in density appears isotropic, while the changes in energy and temperature are pitch angle (Θ) dependent. Between the distributions, $\Delta n_\parallel/n_\parallel = -0.34$ and $\Delta n_\perp/n_\perp = -0.29$ while $\Delta T_\parallel/T_\parallel = +0.02$ and $\Delta T_\perp/T_\perp = +0.10$, where $n_\perp$ and $T_\perp$ are computed from pitch angles $|\Theta - 90°| < 45°$ while $n_\parallel$ and $T_\parallel$ are from $|\Theta - 90°| > 45°$. Protons experience more energization perpendicular to the local magnetic field than parallel. Finally, all three distributions appear

to display a plasma asymmetry between the field-aligned and anti-field-aligned directions, marked approximately by the black arrows. This signature may be due to Mercury's asymmetric loss cones (estimated to be ~10° in the anti-field-aligned direction and ~20° in the field-aligned direction from an offset dipole model; FIPS pitch angle uncertainty is ~10°, for contrast) and/or be an effect of strong planetward flow. Future studies will investigate this signature further.

The typical dipolarization-injection characteristics from superposed epoch analysis agree well with average parameters from all individual events. Each parameter from superposed epoch analysis, save Δt_{GRS}, is within one standard deviation of the histogram means. The duration timescales agree well between the two methods, however, the superposed epoch analysis indicates the injection typically lasts longer than the dipolarization event whereas the histograms indicate the opposite. The close agreement between the average histogram parameters and superposed epoch analysis indicate that although there is considerable spread in dipolarization-injection signatures, as seen in Figure 6, dipolarization-injection events can be well represented with single-value parameters, which may be useful to future modeling studies.

3.3 Spatial frequency & precipitation

To estimate the contribution of dipolarization events to magnetotail injections , we display the spatial fraction of electron events identified within the survey region associated with magnetic field dipolarization in Figure 9. In the same format and binning as Figure 1, Figure 9 examines the spatial distribution of dipolarization events, normalized to the local number of electron events. The dashed white line corresponds to the survey region. The spatial fraction ranges from 0.02 (i.e., 1 dipolarization to 50 electron events) at LT ~ 5.25 and Z_{MSM} ~ 0.35 R_M to 1.00 at LT ~ 0.25 and Z_{MSM} ~ -0.15 R_M. The spatially-averaged fraction of electron events associated with magnetic field dipolarization is 0.25, in contrast to the 538/2976 = 0.18 fraction of electron events within the survey region identified visually with dipolarization signatures.

Compared to the peak electron event frequency in Figure 1, the peak ratio of dipolarizations to electron events is shifted to local times closer to midnight. The distribution of electron events in the magnetotail peak at LT ~ 4, while the peak fraction of electron events associated with dipolarizations occurs at LT ~ 1-2. Above LT ~ 2, the fraction of electron events associated with dipolarization decreases with local time, consistent with the expectation that dipolarization events are confined to the magnetotail and infrequently reach the terminator. Despite the asymmetry of electron events about local midnight, dipolarizations are more associated with events in the post-midnight sector than in the pre-midnight sector. In the post-midnight sector, of the 2732 injections, there were 521 dipolarization-injection events, or approximately 5.2 electron events per dipolarization (i.e., a fraction of 0.19). In the pre-midnight sector, of the 244 electron events, there were 17 dipolarization-injection events, or approximately 14.4 electron events per dipolarization (i.e., a fraction of 0.07). The increased abundance of dipolarization events in the post-midnight

sector is consistent with the observed dawn-dusk asymmetry of dipolarizations at Mercury [*Sun et al.*, 2016].

As Mercury possess large loss cones and lacks an appreciable atmosphere, a portion of the energetic electrons in the dipolarization-injection events are expected to precipitate directly to the planetary surface. Figure 10 depicts the (a) observed and (b) predicted energetic electron precipitation on Mercury's nightside surface. Reproduced in Figure 10a, *Lindsay et al.* [2016] indirectly observed energetic electron precipitation of Mercury's nightside surface; energetic electrons impinging on the surface would produce X-rays detectable by the X-Ray Spectrometer (XRS). *Lindsay et al.* [2016] found a strong dawn-dusk asymmetry in electron precipitation, and with the greatest precipitation occurring just equatorward of the typical open-closed field line boundary [*Korth et al.*, 2015]. In Figure 10b, we compare the expected precipitation from dipolarization-injection events to the precipitation map by *Lindsay et al.* [2016]. Using a simple, azimuthally-symmetric, offset-dipole model of Mercury's magnetic field, we trace MESSENGER's position during each event to Mercury's surface in both hemispheres. Despite the simplicity of the dipole model, the expected precipitation map agrees well with observations from *Lindsay et al.*, particularly in the local time extent of the precipitation and the proximity to the open-closed field line boundary. The disagreement at LT > 4 is due to the azimuthal symmetry of our model.

3.4 Non-dipolarization electron events

Of the 2976 electron events within the survey region, we identified 538 to be associated with magnetic field dipolarization. From the spatial ratio of dipolarization events to electron events, ~25% of injections are directly associated with dipolarization. Compared to the remaining 2438 electron events, the electron events associated with dipolarization tend to reach a higher count rate but last statistically similar durations. The dipolarization-associated events have $<\delta_{peak}>$ = 310 ± 190 s^{-1} and $<\Delta t_{GRS}>$ = 4.4 ± 4.0 s, while the remaining events have $<\delta_{peak}>$ = 160 ± 60 s^{-1} and $<\Delta t_{GRS}>$ = 3.5 ± 5.1 s (after removing outliers). The energy spectra of dipolarization-associated events is statistically indistinguishable from the typical spectra of the remaining events (not shown here), i.e., the remaining events have the same distribution of energies, but fewer counts (particles). Superposed epoch analysis of the remaining electron events, shown in Figure 11, suggests magnetic field dipolarization, or at least plasma sheet thickening, may be common to most magnetotail energetic electron events. Similar to the dipolarization-injection superposed GRS and MAG epoch analysis, we aligned all remaining injections events at the event start time identified by the algorithm and averaged the particle and magnetic field properties. $|B_x|$ and $|B_y|$ show no discernible signatures, however, B_z shows a modest increase (ΔB_z ~ 4 nT) coincident with the increase in GRS count rate, similar to the dipolarization-associated events. The persistent dipolarization signature in the remaining injections suggests that a larger fraction of electron events in Mercury's magnetotail are associated with dipolarization than were identified visually, i.e., >25% of magnetotail electron events appear to be associated with magnetic field dipolarization.

4. Discussion

Using an algorithm to identify energetic electron events in Mercury's magnetotail, we identified 538 magnetic field dipolarizations associated with energetic electron injections and analyzed these events statistically. The average parameters of the dipolarization events, such as the rise time and change in the northward component of the magnetic field, agree well with previous studies of dipolarizations at Mercury. *Sundberg et al.* [2012] identified 24 dipolarization events and found, on average, $<\Delta B_z> = 46$ nT, $<\Delta t_{DF}> = 1.6$ s, $<\Delta t_{DIP}> = 13$ s. We find $<\Delta B_z> = 28.0 \pm 13.3$ nT, $<\Delta t_{DF}> = 2.01 \pm 1.00$ s, and $<\Delta t_{DIP}> = 10.5 \pm 5.4$ s, each agreeing well with events identified by *Sundberg et al.* [2012]. We find a typically smaller $<\Delta B_z>$, however, this is likely due to the small sample size and extreme events analyzed by *Sundberg et al.* [2012]. We also find dipolarization events are more frequent in the post-midnight sector than the pre-midnight sector, despite the strong asymmetry of energetic electron events across the tail, consistent with the spatial distribution of dipolarization fronts identified by *Sun et al.* [2016].

In addition to agreeing well with previous studies at Mercury, the dipolarization characteristics we find at Mercury are similar to those at Earth. From superposed plasma observations, we find a decrease in plasma density within the dipolarization events compared to the ambient plasma, consistent with the interpretation of DFBs as low entropy, depleted plasma bubbles convecting planetward in the magnetotail [e.g., *Pontius and Wolf*, 1990; *Sergeev et al.*, 1996]. Compared to the ambient plasma sheet, we find the typical plasma density inside DFBs is a factor of 0.7 less dense than the ambient plasma, similar to the factor of 0.6 observed at Earth [*Runov et al.*, 2015]. We also find that dipolarization events at Mercury typically exhibit a dip in the magnetic field prior to the step-like increase of the dipolarization front, occasionally with the dip reaching $B_z < 0$ nT, similar to dipolarization events at Earth [e.g., *Slavin et al.*, 2002; *Zhou et al.*, 2014; *Drake et al.*, 2014].

4.1 Particle energization mechanisms during dipolarization events

An important consequence of dipolarization events at Earth is their energization and injection of plasma into the inner magnetosphere. Observations [e.g., *Runov et al.*, 2009, 2013; *Gabrielse et al.*, 2014; *Turner et al.*, 2016] and simulations [e.g., *Ashour-Abdalla et al.*, 2011; *Birn et al.*, 2013, 2014; *Gabrielse et al.*, 2016] of dipolarization events indicate that betatron acceleration (conservation of the first adiabatic invariant) and Fermi acceleration (conservation of the second adiabatic invariant) are the primary acceleration mechanisms for elections. *Birn et al.* [2013], for example, used particle tracing through MHD fields to find that two electron populations are energized by magnetic field dipolarization and contribute to the injection event: (1) electrons drifting across the tail interact with the dipolarization region and experience betatron acceleration; (2) electrons past the magnetotail reconnection site are entrained on newly closed field lines and experience Fermi acceleration as the field line is convected planetward. *Birn et al.* find the first population of electrons is accelerated to greater energies and occurs earlier in the dipolarization event, while finding the second population of electrons is accelerated to relatively lower energies and arrives later during the dipolarization event. Protons, in contrast, experience only quasi-adiabatic betatron acceleration [*Birn et al.*, 2013].

MESSENGER GRS and FIPS observations both indicate that particle acceleration occurs during dipolarization events at Mercury similar to at Earth. The dramatic increase of GRS count rate during dipolarization events suggests electrons are accelerated into the GRS detection limit (estimated to be ~10 keV). Electron energization is corroborated by the superposed GRS spectra, which suggests electrons are accelerated to energies E ~ 130 keV during these events. Although the angular and temporal resolution of the GRS spectrum prevent us from directly observing betatron and Fermi acceleration, the decrease and subsequent sharp increase in GRS count rate coincident with the magnetic field during the dipolarization front suggests the presence of betatron acceleration [e.g., *Runov et al.*, 2013] and the greater proportion of lower energy electrons later during dipolarizations may suggest the presence of Fermi acceleration [*Birn et al.*, 2013].An additional indicator that the dipolarization events, as opposed to magnetic reconnection directly, are accelerating electrons is the location of energetic electron precipitation on Mercury's surface. Particle acceleration during dipolarization events occurs after magnetic reconnection; particles energized by the dipolarization will precipitate equatorward of the open/closed field line boundary [e.g., *Birn et al.*, 2013]. If the electrons were accelerated directly by magnetic reconnection at the reconnection site, then they would precipitate directly onto the open-closed field line boundary. The close agreement between observed and modeled precipitation in Figure 10 equatorward of the open-closed field line boundary indicates that the acceleration is associated with the dipolarization event, and not with magnetic reconnection itself, and that injection events from the magnetotail may be the primary contributors to the nightside energetic electron precipitation.

In contrast to the indirect observations of electron acceleration, plasma observations of H$^+$ exhibit more direct signatures of energization. Using superposed FIPS observations, we find that the thermal H$^+$ plasma contained in dipolarization events has a typical temperature 38.0 MK, compared to the 35.2 MK of the ambient thermal plasma. This increase in energy is dominated by acceleration perpendicular to the magnetic field, i.e., betatron acceleration. We find little field-aligned (Fermi) acceleration. At Earth, ion temperatures observed within DFBs are typically hotter than the ambient plasma sheet by a factor of 1.3 [*Runov et al.*, 2015] as opposed to the factor of 1.1 we find at Mercury. Two case studies analyzed by *Sun et al.* [2017] indicate dipolarizations may heat the plasma by a factor of ~2. While several events reach or exceed this factor (see Figure 6), we find a typically smaller heating factor, which is likely due to the small sample size and extreme events analyzed by *Sun et al.* [2017].

The modest ion acceleration compared to the dramatic electron acceleration is likely an effect of nonadiabatic ion motion. While the energy an individual particle may gain during a dipolarization is highly dependent on its trajectory and interaction with the DF(s) and DFB(s) [e.g., *Gabrielse et al.*, 2016; *Gabrielse et al.*, 2017], we can estimate the typical adiabatic energization. From the average ratio of magnetic field strength at the end of the dipolarization front to the strength at the beginning, we estimate the typical betatron acceleration would increase a particle's perpendicular energy by a factor of ~2.3. From the ratio of dipole field line lengths above Mercury's surface from the typical nightside X-line

location at X_{MSM} = -3 R_M [*Poh et al.*, 2017] to the typical dipolarization-injection event location at L-shell ~ 1.5 R_M, we estimate typical Fermi acceleration would increase a particle's parallel energy by a factor of ~2.7. We expect electrons to behave adiabatically, whereas ions behave nonadiabatically and cannot access these rates of energization fully. For a 47 nT magnetic field (the typical field at the start of the dipolarization front), the H^+ gyroperiod is 1.4 s, whereas the electron gyroperiod is 0.8 ms. With an equatorial pitch angle of 45° at an equatorial distance of 1.5 R_M in a dipole field, the 5 keV H^+ bounce period would be 13.4 s, whereas the 50 keV electron bounce period would be 0.1 s. The H^+ gyro- and bounce periods are on the order of the typical dipolarization front (2.0 s) and dipolarization event (10.5 s) timescales, respectively, indicating nonadiabatic ion motion is expected. *Birn et al.* [2013] found that although proton motion is not strictly adiabatic near dipolarization events at Earth, ions drifting across the dipolarization region are accelerated akin to betatron acceleration, consistent with the acceleration we observe in FIPS observations. Both electrons timescales, in contrast, are significantly shorter than either dipolarization timescale, enabling both betatron and Fermi acceleration. Dipolarization events at Mercury, therefore, may typically only be a powerful source of particle acceleration for electrons.

4.2 Closed drift paths

Closed drift paths, as well as the potential for Mercury's magnetosphere to host radiation belts, have been controversial subjects since Mariner 10's flybys [e.g., *Baker et al.*, 1986]. While the large loss cones and small magnetopause standoff distance prevent permanent radiation belts like at Earth [*Slavin et al.*, 2007], an increasing number of observations at Mercury suggest "quasi-trapped" populations of electrons are able to execute multiple drifts about the planet before being lost to surface precipitation or magnetopause shadowing [e.g., *Ho et al.*, 2016; *Baker et al.*, 2016]. Analytic simulations also suggest the possibility of closed drift paths at Mercury, although they appear to be more Shabansky-like in nature [*Walsh et al.*, 2013].

The GRS superposed epoch analysis appears to have a feature indicative of a closed drift path. Following the dipolarization event, there is a second maxima in the GRS count rate without corresponding features in the magnetic field, suggesting that MESSENGER may be interacting with the injected electrons again as they drift about the planet. Assuming an equatorially-mirroring electron in a dipole field, the electron's energy would need to be ~100 keV to gradient drift about the planet in ~16 s, assuming a dipole moment of 200 nT R_M^3 and an L-shell of 1.6 (corresponding to the typical dipolarization-injection event location). While this energy is within the typical GRS electron energy spectra, the secondary peak is not significant enough to be detected by the algorithm. Additionally, the distribution of electron events about the planet (Figure 1) is consistent with Shabansky orbits; electrons drift near the equatorial latitudes on the nightside and pass through high latitudes in the compressed dayside magnetosphere. Future studies are required to investigate the viability and abundance of energetic electron closed drift paths at Mercury.

4.3 Remaining electron events: Near Mercury Neutral Line

Mercury's northward dipole moment causes electrons to gradient-curvature drift eastward about the planet; electrons injected in the magnetotail would drift to dawn and in the direction of increasing LT. The peak ratio of dipolarizations to electron events at LT ~ 1-2 and the peak electron event occurrence at LT ~ 4-6 are consistent with dipolarization acceleration followed by eastward drift about the planet. As electrons drift about the planet, we expect some to be lost to surface precipitation or magnetopause shadowing, consistent with the decreased counts associated with the remaining injection events compared to the dipolarization-associated events. The remaining events share statistically identical spectra to the dipolarization-associated events, suggesting that the loss process must be energy-independent (e.g., surface precipitation in the loss cone, which may be observed in the superposed FIPS spectra). As electrons continue to drift about the planet, they are expected to be continuously lost to surface precipitation and magnetopause shadowing, while a fraction of electrons may move to higher latitudes on the dayside and participate in a Shabansky orbit [e.g., *Walsh et al.*, 2013], consistent with the global distribution of identified electron events in Figure 1. Without multipoint observations, the Near-Mercury Neutral Line model [e.g., *Baker et al.*, 2016] is difficult to verify, however, the global distribution of electron events, close association of electron events with dipolarizations in the magnetotail, and energy/flux characteristics of events associated and not associated with dipolarization are all consistent with the model. Magnetotail dipolarization may be the dominant source of energetic electron acceleration in Mercury's magnetosphere.

5. Conclusions

We present strong evidence for Mariner 10-like energetic electron injection events associated with magnetic field dipolarization in Mercury's magnetotail. We developed an automated algorithm to identify energetic electron events in the high-time-resolution GRS count rate, and of the 2976 events within the survey region ($X_{MSM} < 0$ R_M and $|Z_{MSM}| < 0.5$ R_M), we associated 538 such events with magnetic field dipolarization signatures. Although individual dipolarization-injection events display large variability in temporal characteristics, statistical analysis reveals a typical dipolarization rise time of ~2 s, during which the northward component of the magnetic field increase by ~30 nT and the energetic electron count rate increases by nearly an order of magnitude. Both the dipolarization and injection would typically last for ~10 s. While these events are observed in the plasma sheet, often close to the central current sheet, dipolarization events occur disproportionally in the post-midnight sector. Both the energetic electron and dipolarization timescales and spatial distributions are consistent with previous studies at Mercury.

We find >25% of magnetotail electron events are associated with magnetic field dipolarization, and observe both direct and indirect electron and ion energization during these dipolarizations. Similar to dipolarization events at the Earth, electrons behave adiabatically and experience both betatron and Fermi acceleration during dipolarization intervals, reaching energies ~130 keV. These electrons contribute to nightside surface precipitation and may drift about the planet in Shabansky-like orbits. Ions, in contrast, are not strictly adiabatic and appear to participate only in modest betatron acceleration. Despite the

only modest energization of ions, the plasma density decreases during dipolarization intervals compared to the ambient plasma sheet, consistent with the interpretation of dipolarization events as low entropy, depleted flux tubes convecting planetward following the collapse of the inner magnetotail. Dipolarization events at Mercury, therefore, may typically only be a powerful source of particle acceleration for electrons.

While only >25% of electron events within the survey region are coincident with magnetic field dipolarization, comparisons between the dipolarization-associated electron events and the remaining events are consistent with the Near-Mercury Neutral Line model of magnetotail injection and eastward drift about the planet [e.g., *Baker et al.*, 2016]. Without multipoint observations, associating the remaining electron events with dipolarization acceleration is nontrivial. If these remaining events are indeed energized by a dipolarization upstream of the spacecraft and subsequently drift to the spacecraft's location, magnetic field dipolarization may be the dominant mechanism for energetic electron acceleration at Mercury. The substantial association between electron events and dipolarization events, the dramatic increase in energetic electron count rate during dipolarization events, the significant precipitation associated with dipolarization-accelerated electrons, and the possibility for these accelerated electrons to transport through the magnetosphere indicate that Mariner 10-like dipolarization events produce a significant component of the energetic particle environment at Mercury. As dipolarization and injection events are intimately related to substorm events at Earth, these results can provide further insight into the character and dynamics of magnetospheric substorm-like events at Mercury, the focus of our future work.

Appendix A. Energetic electron event identification algorithm

The energetic electron detection technique is described briefly in Section 2.2. In this appendix, we discuss the identification procedure in detail. Figure A1a displays an example of the algorithm background (red) determined from the GRS count rate (black) during the 24 May 2013 07:45 magnetospheric pass. The algorithm identified 69 electron events (red arrows) as intervals when the GRS rate exceeds the level of significance (cyan). The two inserts depict the local GRS distribution used to generate the background during two windows, one without electron events (Figure A1b) and one with electron events (Figure A1c).

At native resolution and in the absence of energetic electron events, the (background) GRS count rate is well described by a Poisson distribution with mean and variance λ, dominated by GCRs and planetary neutrons interacting with the anticoincidence shield (see Section 2.1). Smoothing the background count rate with a moving boxcar average, by the central limit theorem, causes the background rate to be approximated by a Gaussian distribution with mean $\bar{x} = \lambda$ and variance $\sigma^2 = \lambda/N_s$, where N_s is the number of points used in the boxcar filter. From Gaussian statistics, knowing $\bar{x}$ and σ allows us to determine significant observations, interpreted as energetic electron events. To complicate this procedure, the background Gaussian distribution is time-dependent (i.e., $\bar{x} = \bar{x}(t)$ and $\sigma = \sigma(t)$) as it responds to both changes in spacecraft altitude and in boresight pointing. While changes in altitude often have timescales of several minutes (e.g., 08:20 to 08:40 in Figure A1a), changes

in spacecraft pointing can change the background rate on the timescale of a minute (e.g., 08:49). By contrast, electron events appear as sharp, localized (timescales of seconds) peaks superposed on the background (e.g., 08:56 to 09:16). To accommodate the time-variable nature of the background, we use a sliding window to find the local background Gaussian distribution and construct the background count rate from the time series of the local Gaussian parameters.

To identify electron events within each MESSENGER orbit, we applied the following procedure to each interval of continuous GRS observations:

1. Smooth the GRS count rate with a moving boxcar average (N_s = 100, i.e., a 1-s smoothing filter).
2. Construct the background count rate in sliding windows of duration t_{window} = 1 min and with a time step between windows Δt_{step} = 0.1 min. Within each window (e.g., as depicted in Figure A1b and Figure A1c), use an iterative Gaussian fit to find the local $\bar{x}$ and σ:
    a. Construct the GRS histogram of counts.
    b. Identify the lowest-count peak within the histogram (e.g., the peak at ~4.2 (10 ms)$^{-1}$ in Figure A1c).
    c. Determine the cumulative number of observations to the left of this peak.
    d. Find the bin to the right of this peak that, between the peak and the bin, contains the same cumulative number of observations as found in step 2c.
    e. Fit a Gaussian to the subset of the histogram spanning the leftmost bin to the bin selected in step 2d. This initial fit returns $\bar{x}_{temp}$ and σ_{temp}.
    f. Using the fit in step 2e as an initial guess, select all histogram bins less than $\bar{x}_{temp} + 2\sigma_{temp}$ and fit a Gaussian to this subset of the histogram, returning a new $\bar{x}_{temp}$ and σ_{temp}. Iteratively repeat this step until the Gaussian fit converges.
    g. Return the local mean $\bar{x} = \bar{x}_{temp}$ and variance $\sigma^2 = \bar{x}_{temp}/N_s$. The black dashed line in Figure A1b and 1c correspond to a Gaussian with mean $\bar{x}$ and variance σ^2. We found the propagated Poisson variance $\sigma^2 = \bar{x}_{temp}/N_s$ to be a more accurate and reliable measure of uncertainty than the returned Gaussian σ^2_{temp}.
3. From all local $\bar{x}$ and σ construct the background time series, $\bar{x}(t)$ and $\sigma(t)$. To ensure a continuous background, apply a 1-min moving boxcar average to $\bar{x}(t)$ and $\sigma(t)$.
4. Find all GRS points that fall above $\bar{x}(t) + 5\sigma(t)$ (cyan in Figure A1a). Aggregate any significant points within 1 s of another (to reduce the total number of events), and record the start and stop times of each bundle of significant points as an electron event.

Over the 1 March 2013 to 30 April 2015 period of our study, the algorithm identified 11756 energetic electron events over 2139 orbits. We removed 214 orbits from our analysis due to high solar energetic particle count rates in the detector. We estimate 1190 (~10%) of the events are false positives, due to anomalously low background fitting. Since the algorithm

identifies the lowest count peak in the GRS histogram (e.g., the leftmost peak in Figure A1c), an anomalously low number of counts will skew the local background low and produce a series of false positive events. Visually checking each orbit and the low rate of false positives suggest the algorithm accurately identified energetic electron events. We validated the algorithm by comparing the duration and amplitude of identified GRS events against synthetic GRS events identified by the algorithm (not shown here) and found no significant systematic bias in the algorithm. The algorithm is validated further by the similarities the spatial distribution of events in Figure 1 shares with previous studies of electron events at Mercury [*Lawrence et al.*, 2015; *Baker et al.*, 2016; *Ho et al.*, 2016].

Acknowledgements

References

Alexeev, I. I., et al. (2010), Mercury's magnetospheric magnetic field after the first two MESSENGER flybys, *Icarus*, **209**, 23–39, doi:10.1016/j.icarus.2010.01.024.

Anderson, B. J., M. H. Acuña, D. A. Lohr, J. Scheifele, A. Raval, H. Korth, and J. A. Slavin (2007), The Magnetometer instrument on MESSENGER, *Space Sci. Rev.*, **131**, 417–450, doi:10.1007/s11214-007-9246-7.

Anderson, B. J., C. L. Johnson, H. Korth, M. E. Purucker, R. M. Winslow, J. A. Slavin, S. C. Solomon, R. L. McNutt Jr., J. M. Raines, and T. H. Zurbuchen (2011), The global magnetic field of Mercury from MESSENGER orbital observations, *Science*, **333**, 1859–1862, doi:10.1126/science.1211001.

Andrews, G. B., et al. (2007), The Energetic Particle and Plasma Spectrometer instrument on the MESSENGER spacecraft, *Space Sci. Rev.*, **131**, 523–556, doi:10.1007/s11214-007-9272-5.

Angelopoulos, V., W. Baumjohann, C. F. Kennel, F. V. Coroniti, M. G. Kivelson, R. Pellat, R. J. Walker, H. Lühr, and G. Paschmann (1992), Bursty bulk flows in the inner central plasma sheet, *J. Geophys. Res.*, **97**, 4027–4039, doi:10.1029/91JA02701.

Ashour-Abdalla, M., M. El-Alaoui, M. L. Goldstein, M. Zhou, D. Schriver, R. Richard, R. Walker, M. G. Kivelson, and K.-J. Hwang (2011), Observations and simulations of non-local acceleration of electrons in magnetotail magnetic reconnection events, *Nat. Phys.*, **7**, 360–365, doi:10.1038/nphys1903.

Baker, D. N., P. R. Higbie, E. W. Hones Jr., and R. D. Belian (1978), High-resolution energetic particle measurements at 6.6 RE 3. Low-energy electron anisotropies and short-term

substorm predictions, *J. Geophys. Res.*, **83**, 4863–4868, doi:10.1029/JA083iA10p04863.

Baker, D. N., J. A. Simpson, and J. H. Eraker (1986), A model of impulsive acceleration and transport of energetic particles in Mercury's magnetosphere, *J. Geophys. Res.*, **91**, 8742–8748, doi:10.1029/JA091iA08p08742.

Baker, D. N., T. I. Pulkkinen, V. Angelopoulos, W. Baumjohann, and R. L. McPherron (1996), Neutral line model of substorms: Past results and present view, *J. Geophys. Res.*, **101**, 12,975–13,010, doi:10.1029/95JA03753.

Baker, D. N., et al. (2016), Intense energetic electron flux enhancements in Mercury's magnetosphere: An integrated view with high-resolution observations from MESSENGER, *J. Geophys. Res. Space Physics*, **121**, 2171–2184, doi:10.1002/2015JA021778.

Birn, J., R. Nakamura, E. V. Panov, and M. Hesse (2011), Bursty bulk flows and dipolarization in MHD simulations of magnetotail reconnection, *J. Geophys. Res.*, **116**, A01, 210, doi:10.1029/2010ja016083.

Birn, J., M. Hesse, R. Nakamura, and S. Zaharia (2013), Particle acceleration in dipolarization events, *J. Geophys. Res. Space Physics*, **118**, 1960–1971, doi:10.1002/jgra.50132.

Birn, J., A. Runov, and M. Hesse (2014), Energetic electrons in dipolarization events: Spatial properties and anisotropy, *J. Geophys. Res. Space Physics*, **119**, 3604–3616, doi:10.1002/2013JA019738.

Christon, S. P., J. Feynman, and J. A. Slavin (1987), Dynamic substorm injections–Similar magnetospheric phenomena at Earth and Mercury, in *Magnetotail Physics*, edited by A. T. Y. Lui, pp. 393–400, Johns Hopkins Univ. Press, Baltimore, Md.

Delcourt, D. C., T. E. Moore, and M.-C. H. Fok (2010), Ion dynamics during compression of Mercury's magnetosphere, *Ann. Geophys.*, **28**, 1467-1474, doi:10.5194/angeo-28-1467-2010.

Deng, X., M. Ashour-Abdalla, M. Zhou, R. Walker, M. El-Alaoui, V. Angelopoulos, R. E. Ergun, and D. Schriver (2010), Wave and particle characteristics of earthward electron injections associated with dipolarization fronts, *J. Geophys. Res.*, **115**, A09,225, doi:10.1029/2009JA015107.

Drake, J. F., M. Swisdak, P. A. Cassak, and T. D. Phan (2014), On the 3-D structure and dissipation of reconnection-driven flow bursts, *Geophys. Res. Lett.,* **41**, 3710-3716, doi:10.1002/2014GL060249.

Fu, H. S., Y. V. Khotyaintsev, M. André, and A. Vaivads (2011), Fermi and betatron acceleration of suprathermal electrons behind dipolarization fronts, *Geophys. Res. Lett.*, **38**, L16104, doi:10.1029/2011GL048528.

Fu, H. S., Y. V. Khotyaintsev, A. Vaivads, A. Retinò, and M. André (2013), Energetic electron acceleration by unsteady magnetic reconnection, *Nat. Phys.*, **9**, 426-430, doi:10.1038/nphys2664.

Gabrielse, C., V. Angelopoulos, A. Runov, and D. L. Turner (2014), Statistical characteristics of particle injections throughout the equatorial magnetotail, *J. Geophys. Res. Space Physics*, **119**, 2512–2535, doi:10.1002/2013JA019638.

Gabrielse, C., C. Harris, V. Angelopoulos, A. Artemyev, and A. Runov (2016), The role of localized inductive electric fields in electron injections around dipolarizing flux bundles, *J. Geophys. Res. Space Physics*, **121**, 9560–9585, doi:10.1002/2016JA023061.

Gabrielse, C., V. Angelopoulos, C. Harris, A. Artemyev, L. Kepko, and A. Runov (2017), Extensive electron transport and energization via multiple, localized dipolarizing flux bundles, *J. Geophys. Res. Space Physics*, **122**, 5059-5076, doi:10.1002/2017JA023981.

Gershman, D. J., et al. (2013), Magnetic flux pile-up and plasma depletion in Mercury's subsolar magnetosheath, *J. Geophys. Res. Space Physics,* **118**, 7181–7199, doi:10.1002/2013JA019244.

Goldsten, J. O., et al. (2007), The MESSENGER Gamma-Ray and Neutron Spectrometer, *Space Sci. Rev.,* **131**, 339–391, doi:10.1007/s11214-007-9262-7.

Ho, G. C., et al. (2011a), MESSENGER observations of transient bursts of energetic electrons in Mercury's magnetosphere, *Science*, **333**, 1865–1868, doi:10.1126/science.1211141.

Ho, G. C., R. D. Starr, R. E. Gold, S. M. Krimigis, J. A. Slavin, D. N. Baker, B. J. Anderson, R. L. McNutt Jr., L. R. Nittler, and S. C. Solomon (2011b), Observations of suprathermal electrons in Mercury's magnetosphere during the three MESSENGER flybys, *Planet. Space Sci.*, **59**, 2016–2025.

Ho, G. C., S. M. Krimigis, R. E. Gold, D. N. Baker, B. J. Anderson, H. Korth, J. A. Slavin, R. L. McNutt Jr., R. M. Winslow, and S. C. Solomon (2012), Spatial distribution and spectral characteristics of energetic electrons in Mercury's magnetosphere, *J. Geophys. Res.*, **117**, A00M04, doi:10.1029/2012JA017983.

Ho, G. C., et al. (2016), MESSENGER observations of suprathermal electrons in Mercury's magnetosphere, *Geophys. Res. Lett.*, **43**, 550–555, doi:10.1002/2015GL066850.

Korth, H., N. A. Tsyganenko, C. L. Johnson, L. C. Philpott, B. J. Anderson, M. M. Al Asad, S. C. Solomon, and R. L. McNutt Jr. (2015), Modular model for Mercury's magnetospheric magnetic field confined within the average observed magnetopause, *J. Geophys. Res. Space Physics*, **120**, 4503–4518, doi:10.1002/2015JA021022.

Lawrence, D. J., et al. (2015), Comprehensive survey of energetic electron events in Mercury's magnetosphere with data from the MESSENGER Gamma-Ray and Neutron Spectrometer, *J. Geophys. Res. Space Physics*, **120**, 2851–2876, doi:10.1002/2014JA020792.

Lindsay, S. T., et al. (2016), MESSENGER X-ray observations of magnetosphere-surface interaction on the nightside of Mercury, *Planet Space Sci.*, **125**, 72-79, doi:10.1016/j.pss.2016.03.005.

Liu, J., V. Angelopoulos, A. Runov, and X.-Z. Zhou (2013), On the current sheets surrounding dipolarizing flux bundles in the magnetotail: The case for wedgelets, *J. Geophys. Res. Space Physics*, **118**, 2000-2020, doi:10.1002/jgra.50092.

Peplowski, P. N., et al. (2015), Geochemical terranes of Mercury's northern hemisphere revealed by MESSENGER neutron measurements, *Icarus*, **253**, 346-363, doi:10.1016/j.icarus.2015.02.002.

Poh, G., et al. (2017), Mercury's cross-tail current sheet: Structure, X-line location and stress balance, *Geophys. Res. Lett.,* **44**, 678-686, doi:10.1002/2016GL071612.

Pontius, D. H. and R. A. Wolf (1990), Transient flux tubes in the terrestrial magnetosphere, *Geophys. Res. Lett.,* **17**, 49-52, doi:10.1029/GL017i001p00049.

Runov, A., V. Angelopoulos, M. I. Sitnov, V. A. Sergeev, J. Bonnell, J. P. McFadden, D. Larson, K.-H. Glassmeier, and U. Auster (2009), THEMIS observations of an earthward-propagating dipolarization front, *Geophys. Res. Lett.*, **36**, L14106, doi:10.1029/2009GL038980.

Runov, A., V. Angelopoulos, and X.-Z. Zhou (2012), Multipoint observations of dipolarization front formation by magnetotail reconnection, *J. Geophys. Res.*, **117**, A05,230, doi:10.1029/2011JA017361.

Runov, A., V. Angelopoulos, C. Gabrielse, X.-Z. Zhou, D. Turner, and F. Plaschkle (2013), Electron fluxes and pitch-angle distributions at dipolarization fronts: THEMIS multipoint observations, *J. Geophys. Res. Space Physics*, **118**, 744-755, doi:10.1002/jgra.50121.

Runov, A., V. Angelopoulos, C. Gabrielse, J. Liu, D. L. Turner, and X.-Z. Zhou (2015), Average thermodynamic and spectral properties of plasma in and around dipolarizing flux bundles, *J. Geophys. Res. Space Physics*, **120**, 4369-4383, doi:10.1002/2015JA021166.

Schlemm, C. E., II, et al. (2007), The X-Ray Spectrometer on the MESSENGER spacecraft, *Space Sci. Rev.*, **131**, 393–415.

Sergeev, V. A., V. Angelopoulos, J. T. Gosling, C. A. Cattell, and C. T. Russell (1996), Detection of localized, plasma-depleted flux tubes or bubbles in the midtail plasma sheet, *J. Geophys. Res.*, **101**, 10,817–10,826, doi:10.1029/96JA00460.

Simpson, J. A., J. H. Eraker, J. E. Lamport, and P. H. Walpole (1974), Electrons and protons accelerated in Mercury's magnetic field, *Science*, **185**, 160–166.

Slavin, J. A., et al. (2002), Simultaneous observations of earthward flow bursts and plasmoid ejection during magnetospheric substorms, *J. Geophy. Res.*, **107**(A7), SMP 13-1–SMP 13-23, doi:10.1029/2000JA003501.

Slavin, J. A., et al. (2007), MESSENGER: Exploring Mercury's magnetosphere, *Space Sci. Rev.*, **131**, 133–160, doi:10.1007/s1/214-007-9154-x.

Slavin, J. A., et al. (2009), MESSENGER observations of magnetic reconnection in Mercury's magnetosphere, *Science*, **324**, 606-610, doi:10.1126/science.1172011.

Slavin, J. A., et al. (2010), MESSENGER observations of extreme loading and unloading of Mercury's magnetic tail, *Science*, **329**, 665–668, doi:10.1126/science.1188067.

Slavin, J. A., et al. (2012), MESSENGER and Mariner 10 flyby observations of magnetotail structure and dynamics at Mercury, *J. Geophys. Res.*, **117**, A01215, doi:10.1029/2011JA016900.

	Example	Average	Superposed

Sun, W.-J., et al. (2015), MESSENGER observations of magnetospheric substorm activity in Mercury's near magnetotail, *Geophys. Res. Lett*., **42**, 3692–3699, doi:10.1002/2015GL064052.

Sun, W. J., S. Y. Fu, J. A. Slavin, J. M. Raines, Q. G. Zong, G. K. Poh, and T. H. Zurbuchen (2016), Spatial distribution of Mercury's flux ropes and reconnection fronts: MESSENGER observations, *J. Geophys. Res. Space Physics*, **121**, doi:10.1002/2016JA022787.

Sun, W. J., et al. (2017), MESSENGER observations of the energization and heating of protons in the near-Mercury magnetotail, *Geophys. Res. Lett.*, doi:10.1002/2017GL074276.

Sundberg, T., et al. (2012), MESSENGER observations of dipolarization events in Mercury's magnetotail, *J. Geophys. Res.*, **22**, A00M03, doi:10.1029/2012JA017756.

Turner, D. L., et al. (2016), Energy limits of electron acceleration in the plasma sheet during substorms: A case study with the Magnetospheric Multiscale (MMS) mission, *Geophys. Res. Lett.*, **43**, 7785–7794, doi:10.1002/2016GL069691.

Walsh, B. M., A. S. Ryou, D. G. Sibeck, and I. I. Alexeev (2013), Energetic particle dynamics in Mercury's magnetosphere, *J. Geophys. Res. Space Physics*, **118**, 1992-1999, doi:10.1002/jgra.50266.

Zelenyi, L., M. Oka, H. Malova, M. Fujimoto, D. Delcourt, and W. Baumjohann (2007), Particle acceleration in Mercury's magnetosphere, *Space Sci. Rev.*, **132**, 593–609, doi:10.1007/s11214-007-9169-3.

Zhou, X.-Z., V. Angelopoulos, J. Liu, A. Runov, and S.-S. Li (2014), On the origin of pressure and magnetic perturbations ahead of dipolarization fronts, *J. Geophys. Res. Space Physics*, **119**, 211–220, doi:10.1002/2013JA019394.

Table 1. Example (Figures 2 through 5), average (Figure 6), and superposed epoch (Figure 7) characteristic dipolarization-injection parameters.

	Parameter	07-11-2014T13	04-23-2013T07	07-19-2013T00	07-11-2014T21		
MAG	ΔB_z (nT)	78.3	95.5	20.3	85.8	28.0	19.8
	Δt_{DF} (s)	2.55	0.90	2.60	1.35	2.01	1.75
	Δt_{DIP} (s)	21.2	13.0	20.9	15.9	10.5	8.2
GRS	δ_{peak} (s^{-1})	5920	2670	5840	370	310	450
	E_{peak} (keV)	180	140	210	80	120	130
	Δt_{GRS} (s)	13.3	15.6	14.9	2.0	4.4	11.0
FIPS	$\Delta n /n$	-1.00	-0.76	-0.46	-0.46	-0.23	-0.30
	$\Delta T /T$	—	0.78	0.12	0.28	0.20	0.08
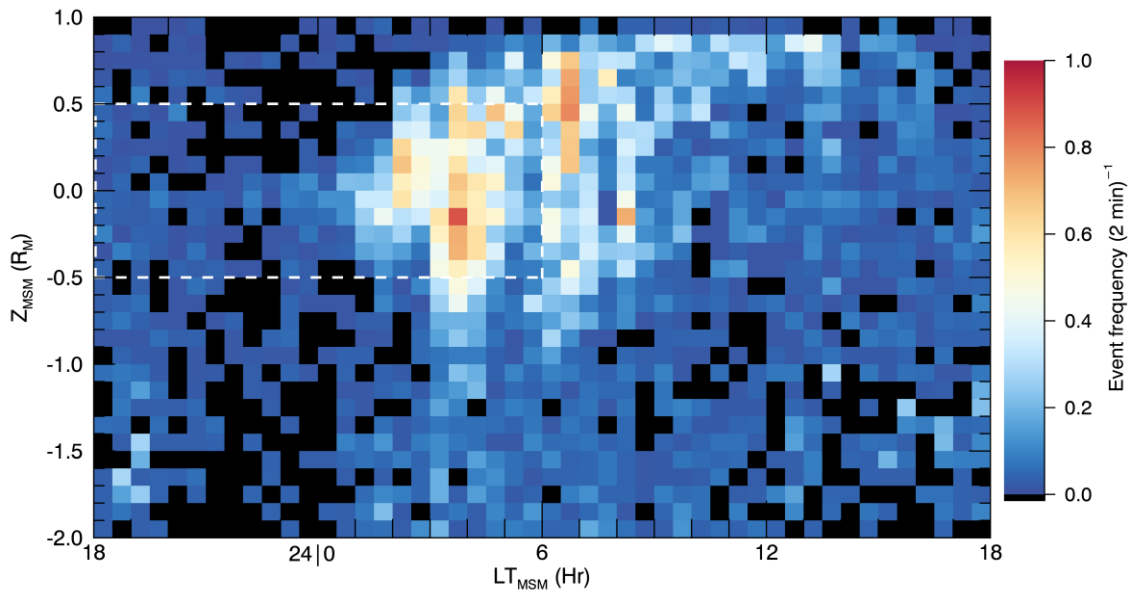
Figure 1. Spatial distribution of GRS electron events identified by the automated algorithm. The color bar indicates the event frequency within each bin of local time (LT, hours) and Z_{MSM} (R_M). Black indicates no identified electron events. The regions enclosed by the dashed white lines correspond to the survey region used to identify dipolarization events.
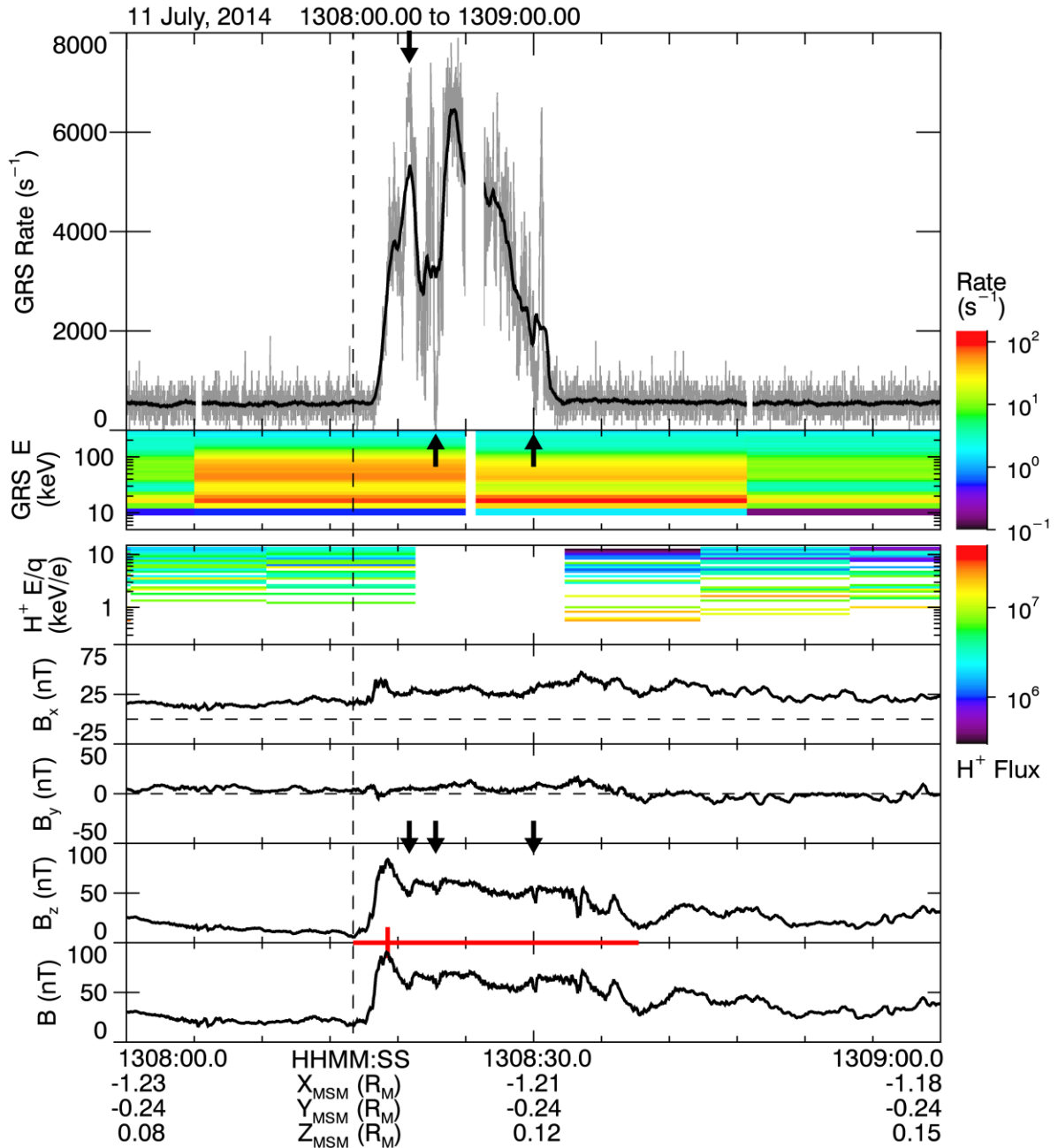
Figure 2. A single dipolarization-injection event. The panels from top to bottom are: GRS count rate, GRS accumulated spectra, FIPS H⁺ flux spectrogram, MAG magnetic field components (B_x, B_y, B_z), and magnetic field strength. The top panel contains both the (thick black line) GRS count rate smoothed by a 1-s moving boxcar average, as specified in the algorithm, and for comparison, the (grey) unsmoothed count rate. The upper color bar indicates count rate in the GRS spectral accumulations; white indicates GRS deadtime or no observed counts. The lower color bar indicates differential H⁺ flux (s^{-1} cm^{-2} keV^{-1} Sr^{-1}); white indicates no observed counts in the H⁺ spectrogram. The spacecraft position in MSM coordinates is listed at the bottom. The vertical dashed line indicates the start of the dipolarization front, the horizontal red line spans the dipolarization event with a vertical tick at the

end of the dipolarization front, the horizontal dashed lines indicate 0 nT, and the arrows denote features discussed in the text.
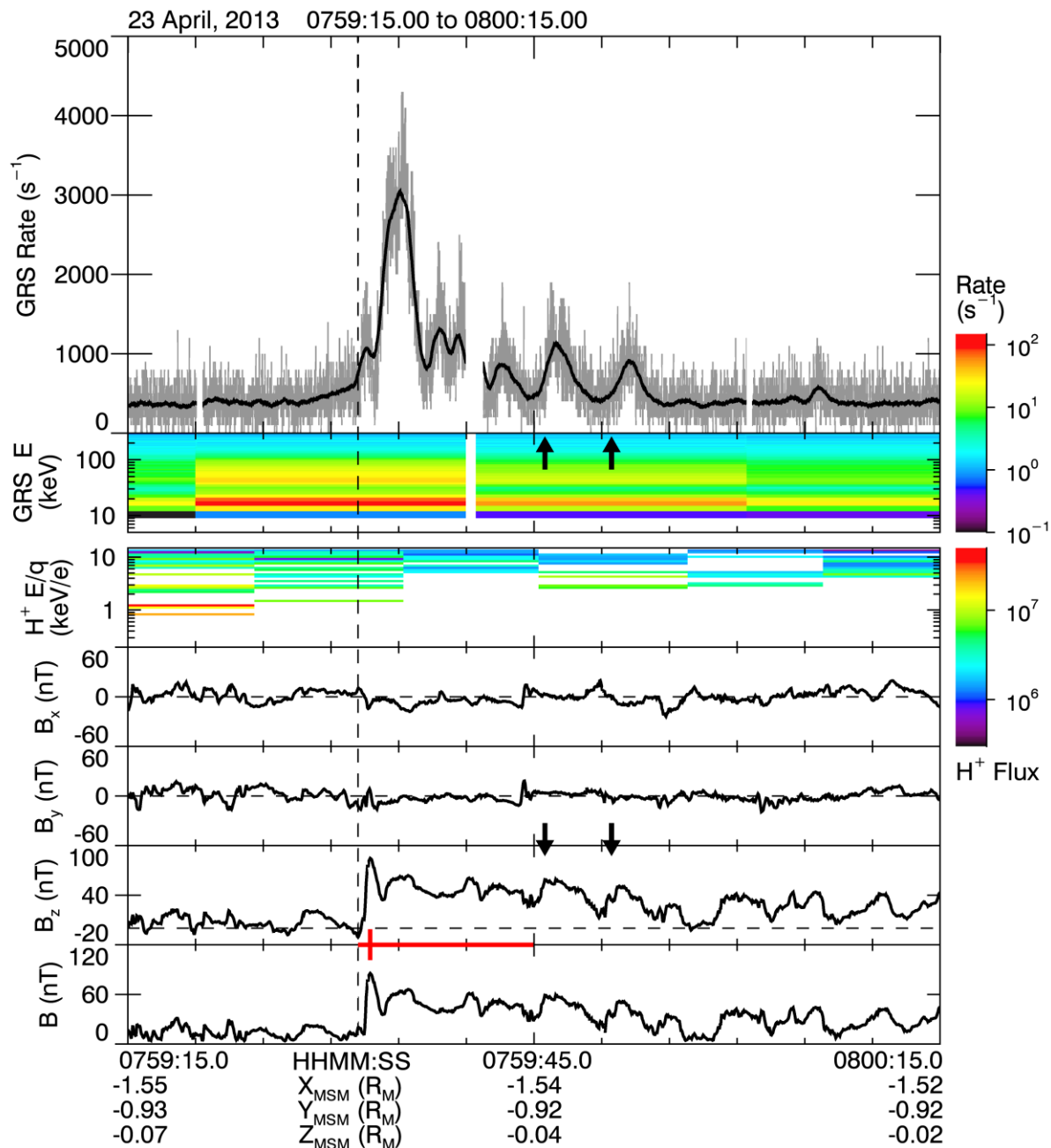
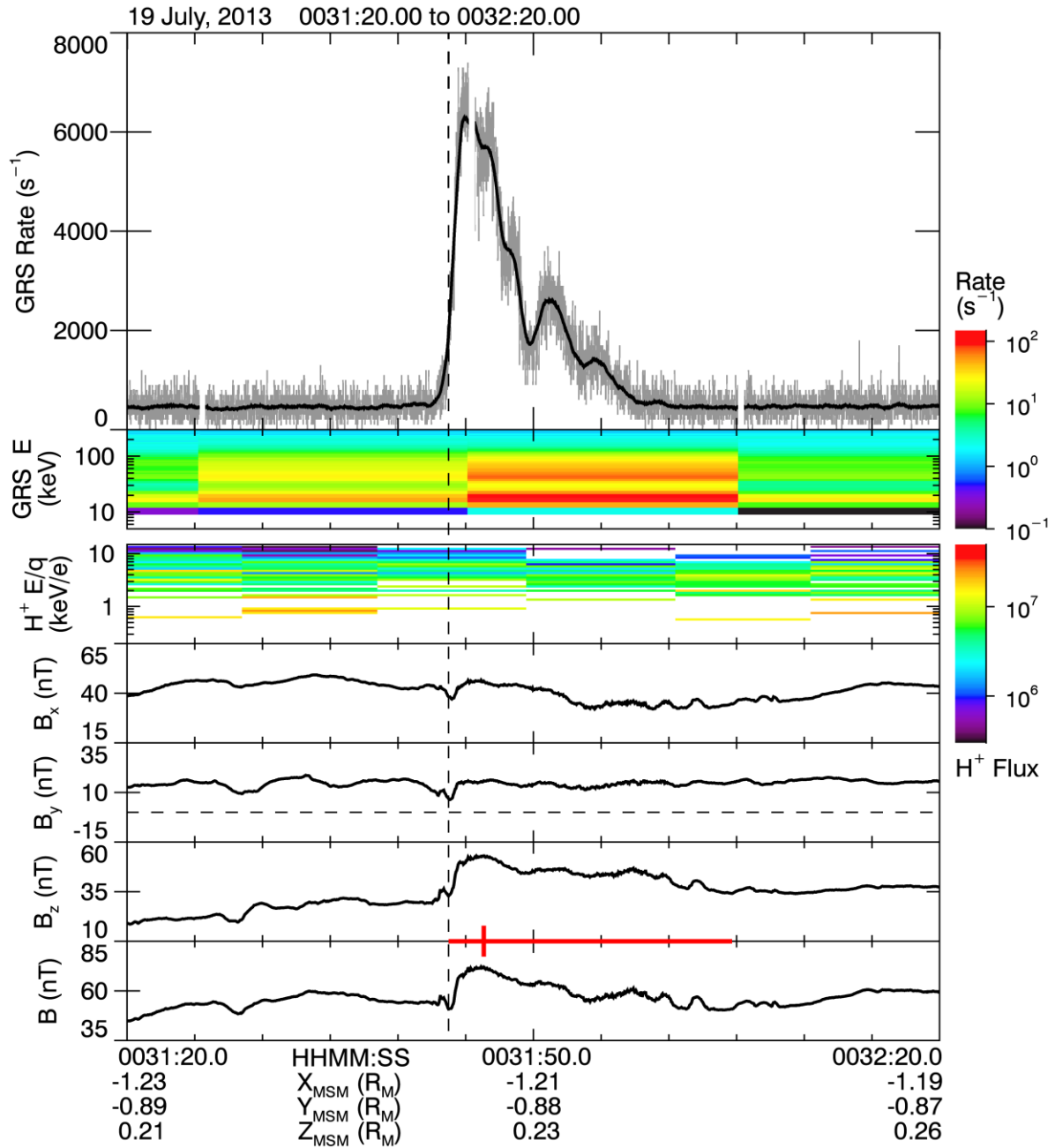**Figure 3.** A series of dipolarization-injection events, in the same format as Figure 2.

Figure 4. A strong injection accompanied by a modest dipolarization, in the same format as Figure 2.
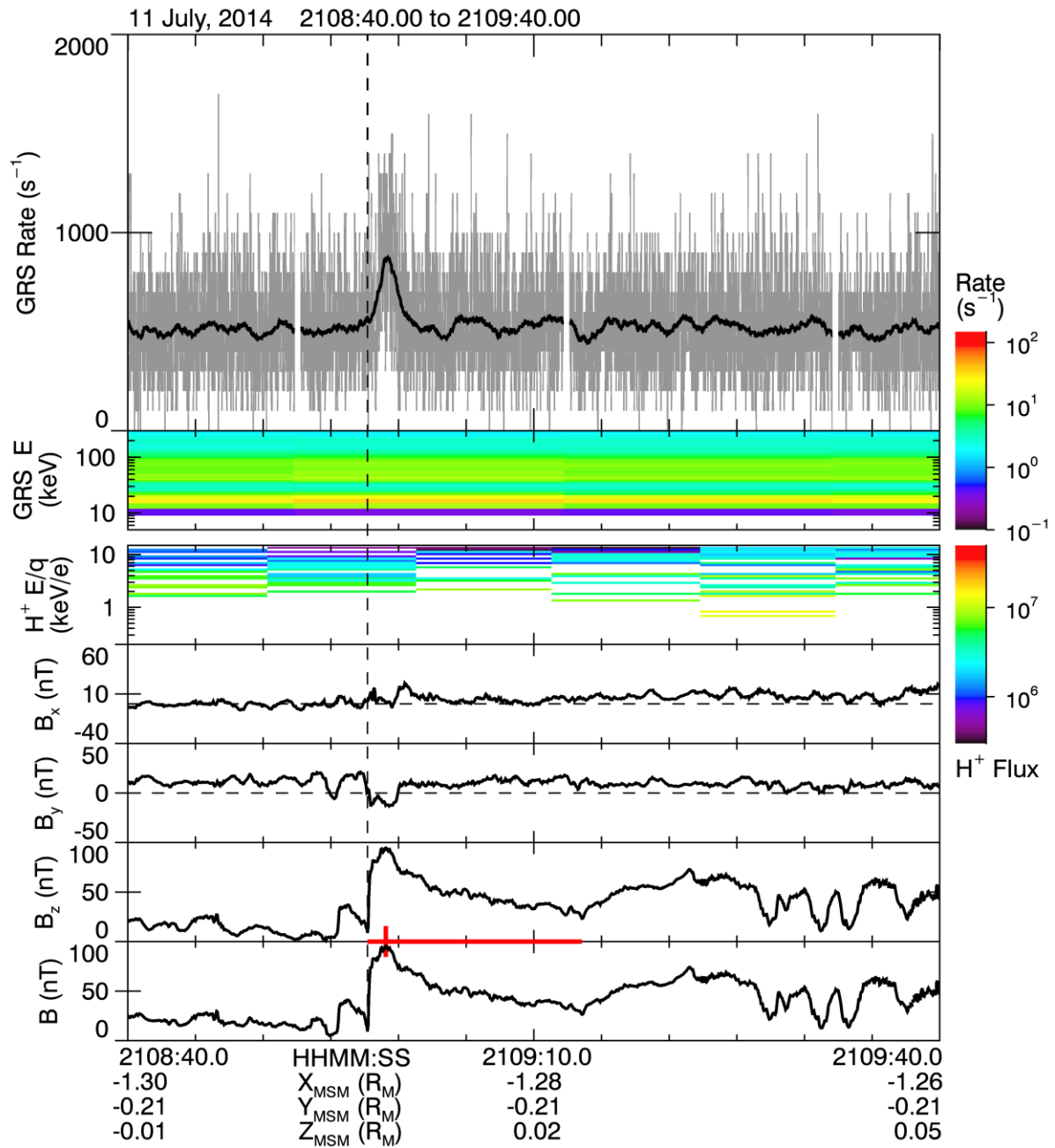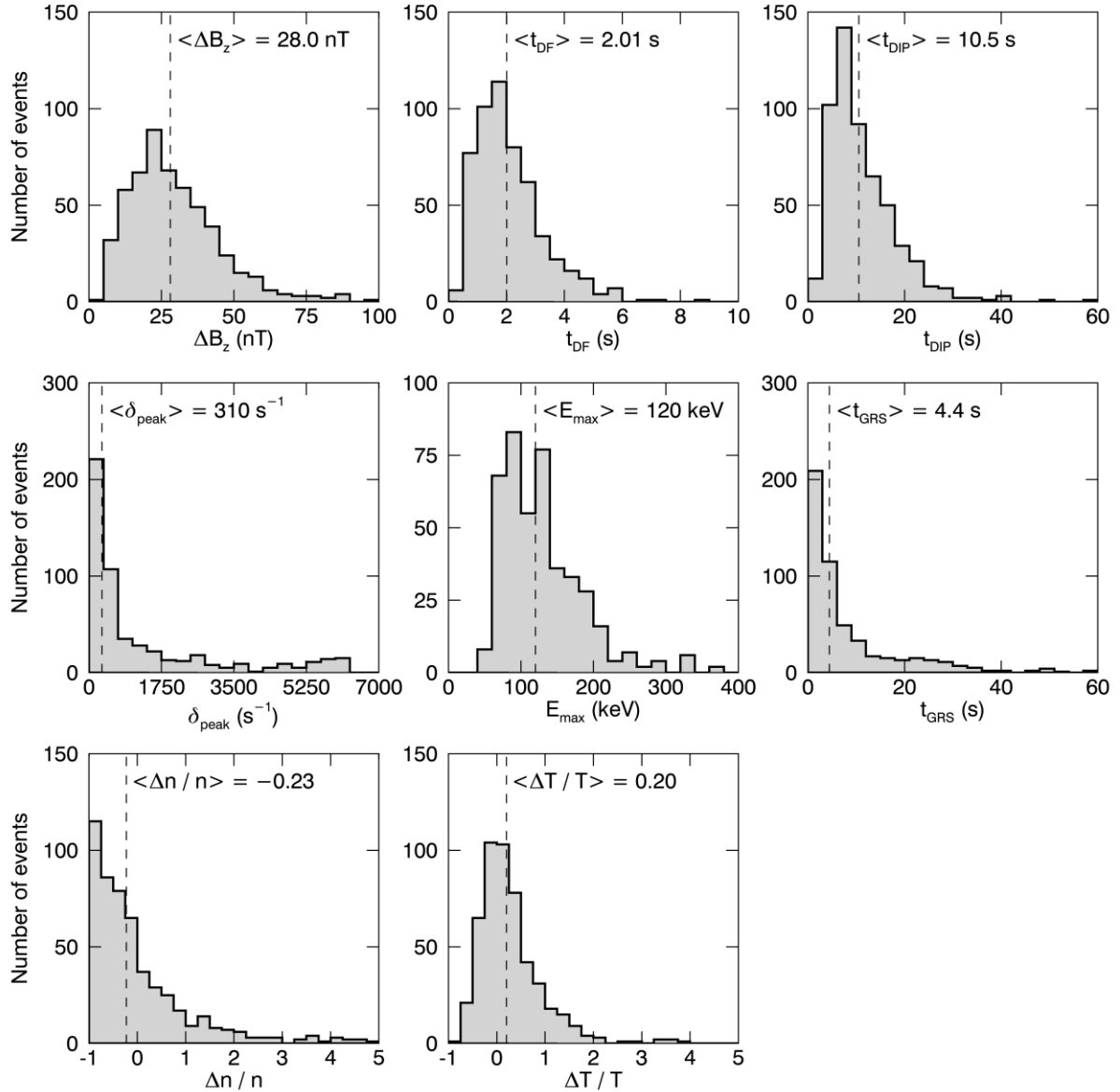
Figure 5. A modest injection accompanied by a strong dipolarization, in the same format as Figure 2.

Figure 6. Histograms of characteristic parameters across all 538 dipolarization-injection events. From left to right: (top row) change in B_z over the dipolarization front, duration of the dipolarization front, and duration of the dipolarization event; (middle row) peak detrended GRS count rate during the injection, maximum electron energy during the injection, and duration of the injection; (bottom row) observed changes in thermal H^+ density and temperature from the ambient plasma to the dipolarizing flux bundle. The mean of each distribution without outliers removed is marked by the dashed line and listed at the top of each panel.
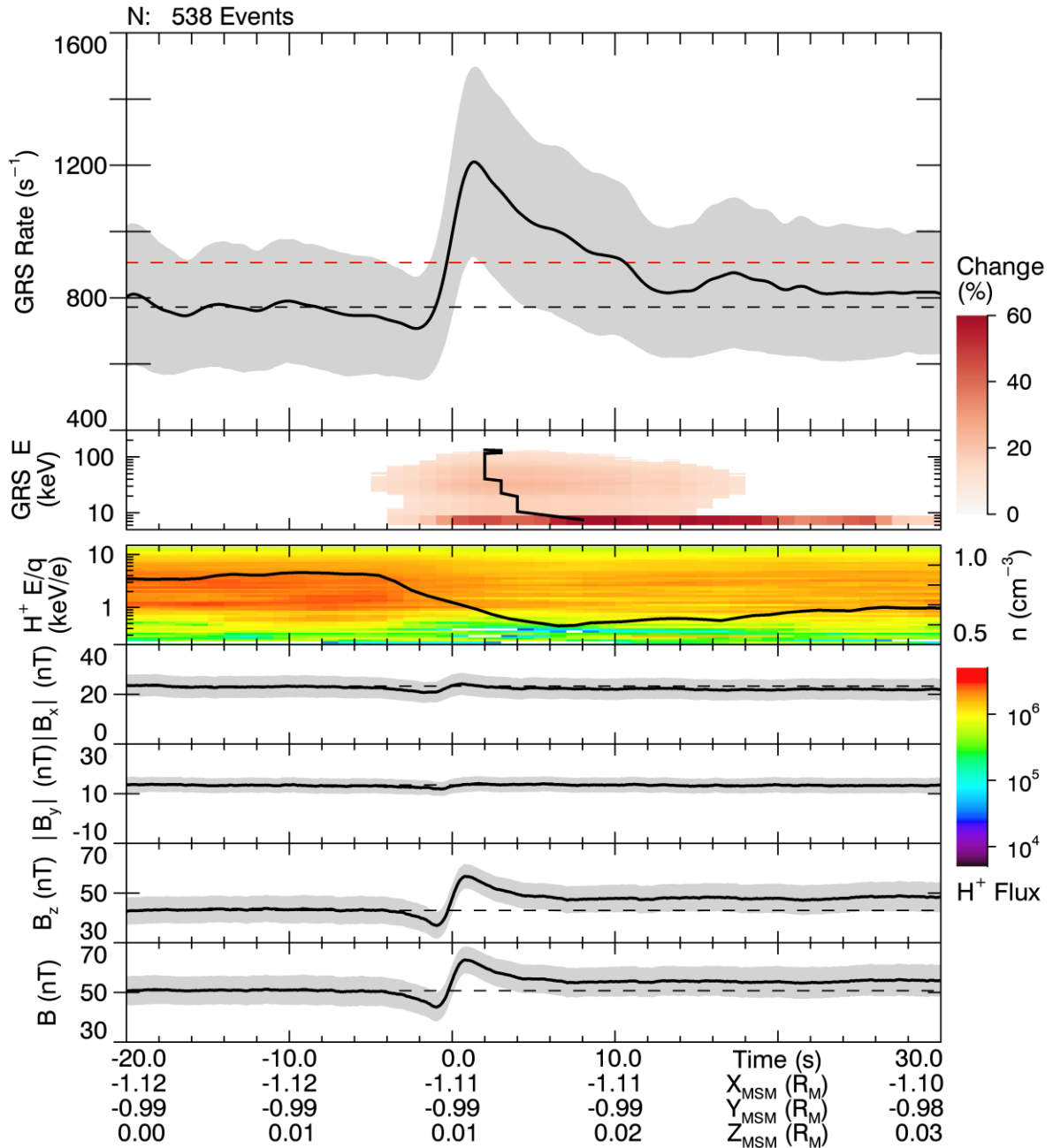
Figure 7. Superposed GRS and MAG epoch analysis in the same general format as Figure 2. All 538 dipolarization events were aligned at the midpoint of the dipolarization front ($t = 0$ s). The second panel corresponds to the relative change in the GRS spectra from the average spectra over $-20 < t < -10$ s. Statistically significant changes are indicated by the upper color bar; relative changes below 3-sigma significance are shaded white. The black line traces the time of maximum percent change at each energy. The third panel includes the proton density, as indicated by the right axis. The fourth and fifth panels correspond to the averaged magnitudes of B_x and B_y across all events, respectively. The horizontal black dashed lines in the GRS rate and MAG panels correspond to the mean value averaged over $-30 \leq t \leq -5$ s. The red dashed line corresponds to the algorithm significance level. The grey

shaded regions correspond to the standard deviation of the mean inflated by a factor of 5. The spacecraft position below the last panel is the average spacecraft location during the dipolarization events.
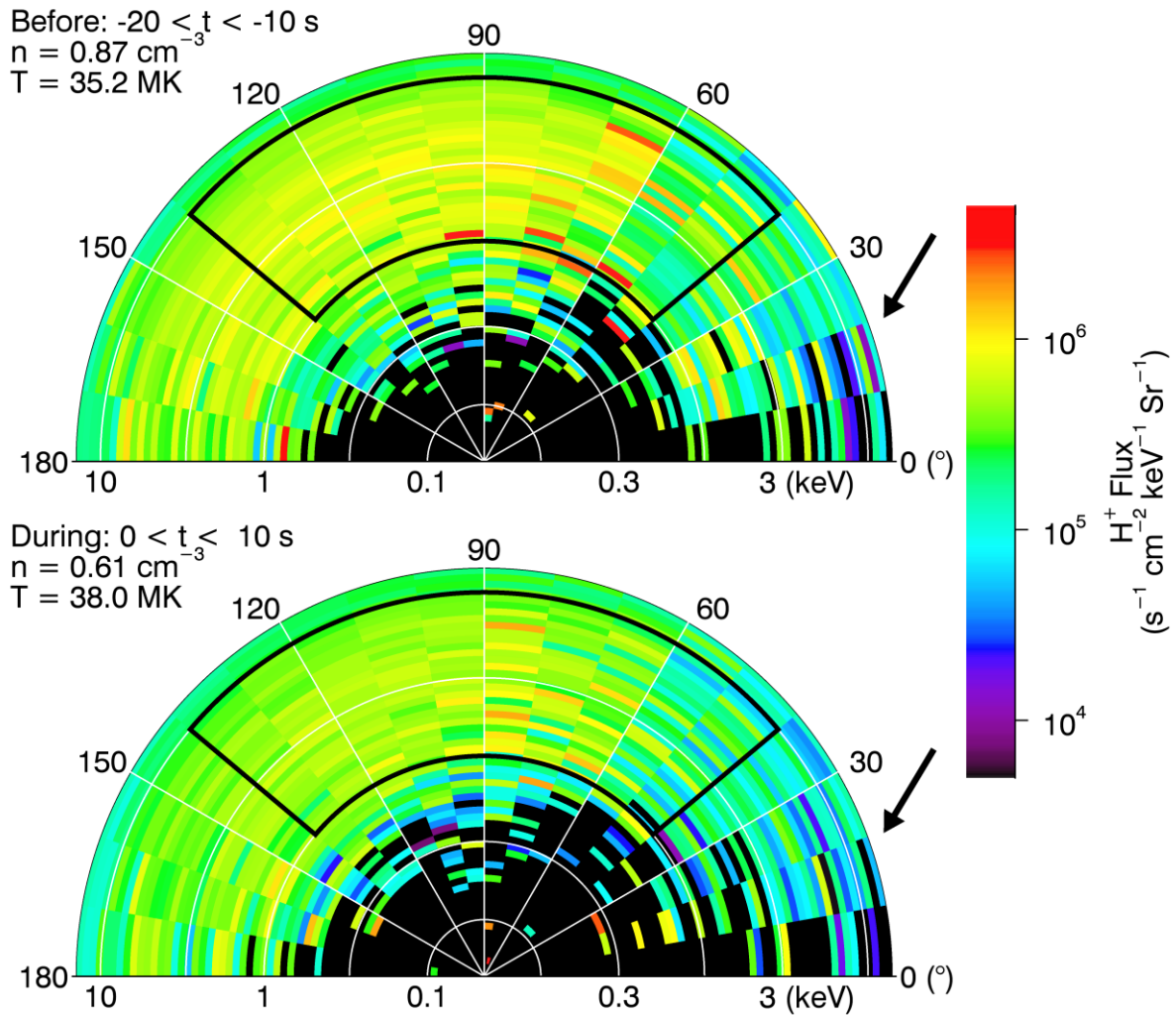

Figure 8. Energy-resolved pitch angle H⁺ distributions from superposed FIPS analysis (top) prior to and (bottom) during the dipolarization event. The radial spokes correspond to the pitch angle and the concentric rings correspond to H⁺ energy. Color bins have nonzero flux as indicated by the color bar. The density and energy moments are listed to the left of each distribution. The arrows and black boxes indicate features discussed in the text.
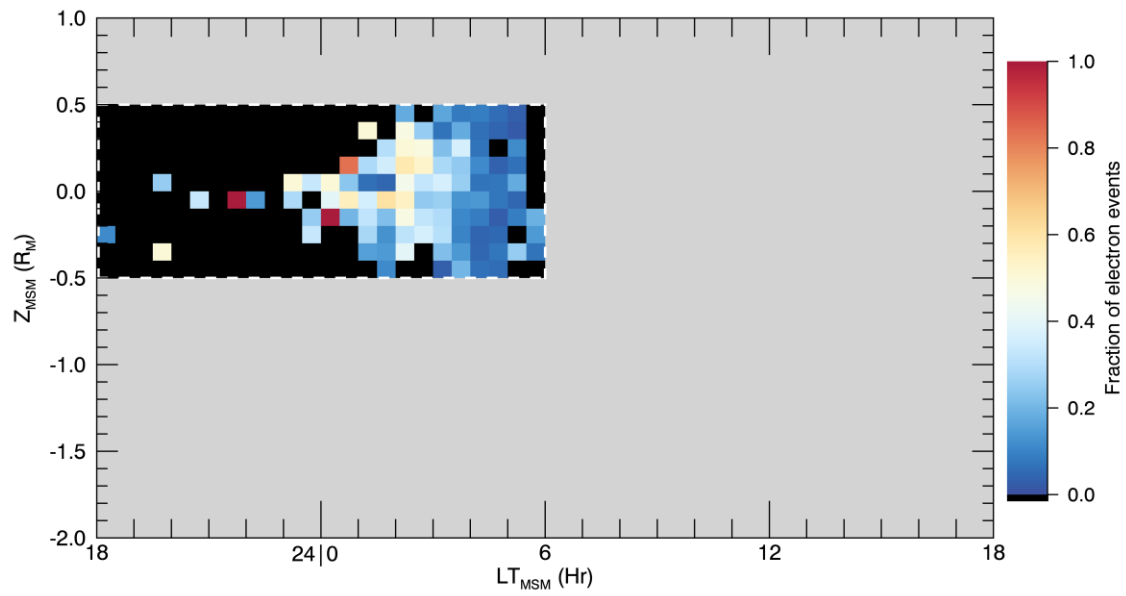
Figure 9. Spatial distribution of the fraction of injection events coincident with magnetic field dipolarization, in the same format as Figure 1. The grey space is outside of the survey region. The color bar indicates the value within each bin. Black indicates locations where no injections were identified (see Figure 1).
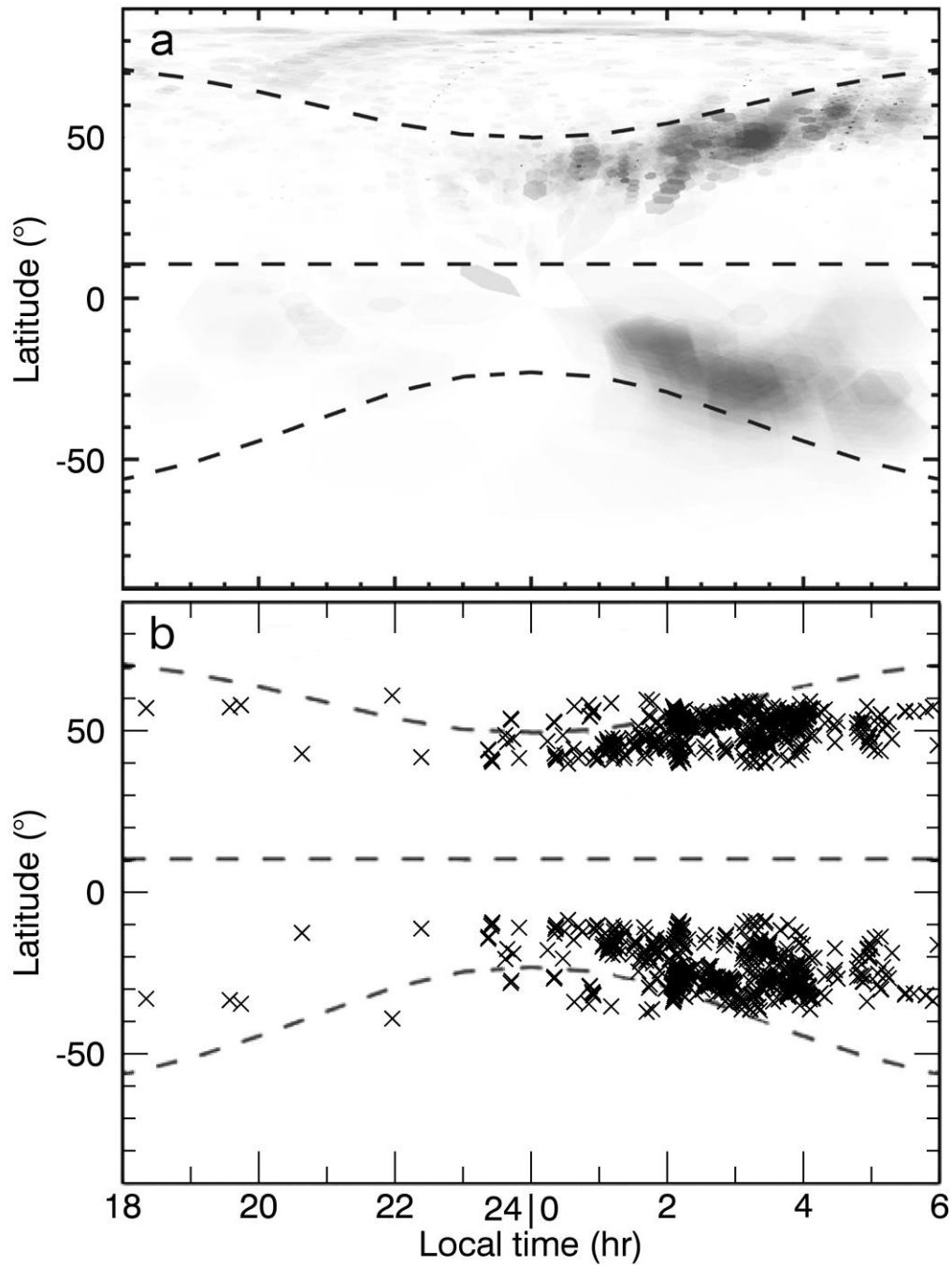
Figure 10. (a) XRS observations of energetic electrons precipitating to Mercury's nightside surface in geographic coordinates, adapted from *Lindsay et al.* [2016]. The dashed lines correspond to the open-closed field line boundary and magnetic equator determined by *Korth et al.* [2015]. (b) The predicted precipitation of energetic electrons during dipolarization-injection events.
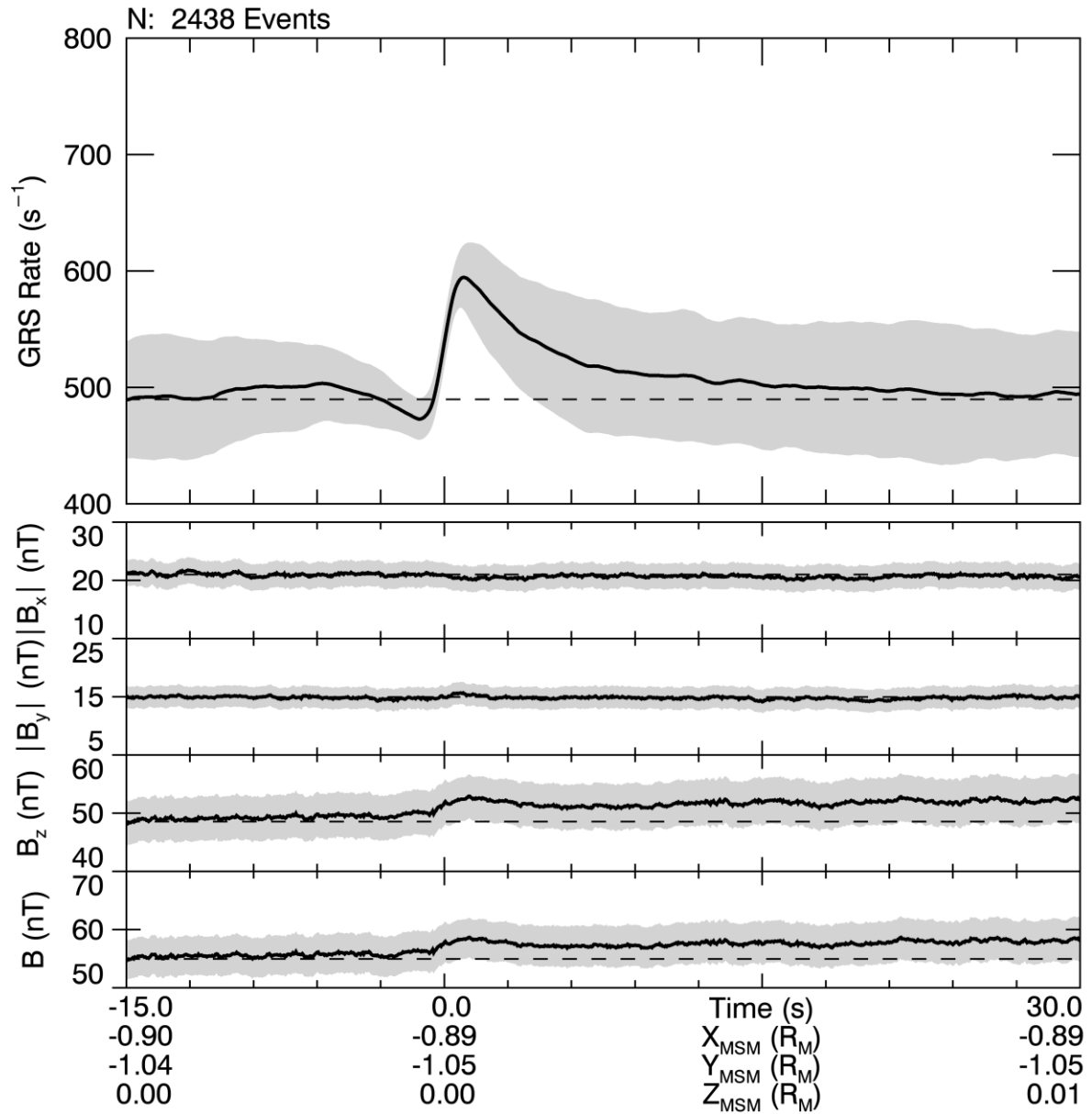
Figure 11. Superposed GRS and MAG epoch analysis of the remaining 2438 electron events within the survey region, in the same format as Figure 7 but with GRS spectral accumulations and FIPS observations removed.